Geomagnetic Storms Driven by Fast Solar Winds and Their Effects on Ultrarelativistic Electrons in the Van Allen Belts

Master's thesis
University of Turku
Physics
May 2021
B.Sc. Christian Palmroos
Examiners:
Dr. Jan Gieseler
Prof. Rami Vainio

According to the University of Turku quality control specifications, this text has been checked with Turnitin Originality Check.

UNIVERSITY OF TURKU
Department of Physics and Astronomy

Palmroos, Christian Geomagnetic Storms Driven by Fast Solar Winds and Their Effects on Ultrarelativistic Electrons in the Van Allen Belts

Master's thesis, 66 p.
Physics
May 2021

The Van Allen belts, also known as radiation belts, are torus-shaped swarms of charged particles trapped in the magnetic field of the Earth. These belts have a two-layer structure, with the comparatively stable inner belt consisting of ions and lower energy electrons, and the outer much more dynamic belt consisting of energetic electrons.

Geomagnetic storms are temporary perturbations in the geomagnetic field and they are known to affect the charged particles trapped in the radiation belts. A geomagnetic storm could be initiated by a coronal mass ejection hitting the Earth's protective magnetic shield, or by a fast flow of solar wind following a stream interaction region. In this thesis, we study a set of geomagnetic storms driven by fast streams of solar wind and the effects these storms had on the energetic electrons in the outer radiation belt.

We employ electron intensity observations made by Aalto-1, PROBA-V, and the Van Allen Probes. Aalto-1 is a university student-built CubeSat and the first Finnish satellite in space. PROBA-V (Project for On-Board Autonomy-Vegetation) is the third satellite of the PROBA family, operated by the European Space Agency (ESA). The Van Allen Probes are twin satellites specifically designed for harsh radiation environments, operated by the National Aeronautics and Space Administration (NASA). We also use OMNI data for interplanetary plasma conditions and the *Dst* index, by which we identify geomagnetic storms. Our dataset covers the autumn of 2017, from October to December.

During some the geomagnetic storms in our dataset, we find both expansion of the outer belt and increase in the measured electron intensities. We find dramatic depletions of the outer belt, related to the main phases of geomagnetic storms. We also find changes in the electron energy spectrum during storm time. The energy spectrum is even found to be noticeably softened for an extended time period in the aftermath of a geomagnetic storm.

Keywords: Van Allen Belts, Radiation Belts, Geomagnetic Storms, Magnetosphere, Space Physics, Energetic Particle Measurements

TURUN YLIOPISTO
Fysiikan ja tähtitieteen laitos

Palmroos, Christian Nopeiden aurinkotuulen virtausten aiheuttamien geomagneettisten myrskyjen vaikutukset Van Allenin vyöhykkeiden ultrarelativistisiin elektroneihin

Pro Gradu, 66 s.
Fysiikka
Toukokuu 2021

Van Allenin vyöhykkeet, tunnetaan myös nimellä säteilyvyöt, ovat toroidin muotoiset varattujen hiukkasten parvet, jotka ovat ansassa Maan magneettikentässä. Näitä vyöhykkeitä on sisäkkäin kaksi. Sisempi vyöhyke on stabiilimpi, ja se koostuu pääasiassa ioneista ja elektroneista. Ulompi vyöhyke on paljon dynaamisempi, ja se koostuu lähinnä korkeaenergisistä elektroneista.

Geomagneettiset myrskyt väliaikaisia häiriöitä Maan magneettikentässä, ja ne tunnetusti vaikuttavat Van Allenin vyöhykkeiden hiukkasiin. Geomagneettinen myrsky voi alkaa koronan massapurkauksen osumasta Maan suojaavaan magneettikenttään, tai nopeista aurinkotuulen virtauksista. Tässä tutkielmassa tutkitaan nopeiden aurinkotuulen virtausten aiheuttamia geomagneettisia myrskyjä, ja näiden vaikutuksia uloimman Van Allenin vyöhykkeen korkeaenergisiin elektroneihin.

Käytämme elektronimittausdataa Aalto-1 satelliitista, PROBA-V satelliitista, ja Van Allenin luotaimista. Aalto-1 on suomalaisten yliopisto-opiskelijoiden rakentama Cube-satelliitti, ja ensimmäinen suomalainen satelliitti avaruudessa. PROBA-V (Project for On-Board Autonomy-Vegetation) on Euroopan avaruusjärjestön (ESA) operoima PROBA-perheen kolmas satelliitti. Van Allenin luotaimet ovat identtiset kaksossatelliitit, jotka on suunniteltu äärimmäisiin hiukkassäteilyn ympäristöihin. Van Allenin luotaimia operoi Yhdysvaltojen ilmailu -ja avaruushallintovirasto (NASA). Tutkielmassa käytämme myös OMNI datasettiä interplanetaaristen olosuhteiden ja $Dst-$indeksin tarkkailua varten. Käytämme $Dst-$indeksiä magneettisten myrskyjen ajankohtien identifiointiin. Datasettimme kattaa syksyn 2017 lokakuusta joulukuuhun.

Tutkielmassa löydämme geomagneettisten myrskyjen ajalta ulomman Van Allenin vyöhykkeen laajenemista, ja elektroni-intensiteettien kasvua. Havaitsemme dramaattisia ulomman vyöhykkeen tyhjenemisiä, jotka liittyvät magneettisten myrskyjen päävaiheisiin. Löydämme myös vaihtelua elektronien energiaspektrissä magneettisten myrskyjen aikana. Elektronien energiaspektri havaittavasti pehmenee pitkäksi aikaa erään geomagneettisen myrskyn jälkeen.

Asiasanat: Van Allenin vyöhykkeet, Säteilyvyöt, Geomagneettiset myrskyt, Magnetosfääri, Avaruusfysiikka, Korkeaenergisten hiukkasten mittaukset

Contents

1 Introduction

The Solar System is a dynamic and gravitationally bound structure in which everything orbits, either directly or indirectly, the common center of mass. We call the space within the Solar System the interplanetary space, to differentiate between, e.g. the interstellar space, which is the space between stars. Our central star, the Sun, acts as a constant source of ionized gas streaming radially outward to fill the interplanetary space. This constant flow of charged particles coming from the Sun, which are in a state of plasma, is called the *solar wind* (SW). Parker (1958) proposed the idea of the extremely hot solar corona expanding at a supersonic speed to explain the mechanism required to produce over a 1000 km/s streams of plasma in the interplanetary space. He correctly concluded that the corona, being in a temperature of $T \sim 10^6$ K, cannot possibly remain in a state of equilibrium, but instead has to either collapse or expand. However, the solar magnetic field constrains the expansion of the corona, so that it's not spherically symmetric. Furthermore, the complex topology of the solar magnetic field evolves over the solar cycle, causing the expansion of the corona to depend of the phase of the solar cycle.

The solar wind streaming away from the Sun at low latitudes is called slow solar wind and it leaves the corona through structures called helmet streamers. Helmet streamers are effectively magnetic loops rising up from the Sun, which accumulate hot plasma into them. The slow solar wind generally has a speed of roughly 350 km/s, while the fast solar wind flows with a speed of $\sim$ 750 km/s (Koskinen, 2011). Slow solar wind is slower and more dense than the fast solar wind and in quiet times it's constrained to the vicinity of the ecliptic plane. Fast solar wind flows out of magnetic field lines, which close in somewhere very far from the Sun. Such field lines are called open field lines. Open field lines can be found from almost all around the Sun, except for at low latitudes. This is exactly the reason, why in the region where most of the matter orbits the Sun, which is the ecliptic plane and its

surroundings, slow solar wind is so much more common than fast solar wind. There are, however, other sources of fast solar wind that direct fast solar wind flows also to the ecliptic plane. Coronal holes are regions of the solar corona, where temperature and density of plasma are lower than the surroundings. From coronal holes the solar magnetic field lines may extend very far, rather than close in near the surface as they normally would. The open field lines emerging up from coronal holes allow for fast solar wind to flow along the field lines. Since coronal holes can form also at low latitudes, so too can fast solar wind flow to the ecliptic plane through them (Koskinen, 2011; Richardson, 2018).

The solar magnetic field is carried within the plasma leaving the Sun, thus forming the interplanetary magnetic field (IMF). Solar wind flows radially outward, and since the Sun is constantly rotating, the magnetic field carried along gets wound up in an Archimedean spiral, which in this context is known as the Parker spiral (Parker, 1958). The solar magnetic field is quite complex, but a view from afar reveals that it does have a kind of north and south polarity. In the vicinity of the ecliptic plane the polarity undergoes a change from north to south and it is there that the *heliospheric current sheet* (HCS) is formed. It is commonly known that the magnitude of a magnetic field decreases as $B \propto r^{-2}$. Thus it would be reasonable to assume this to be the case for the IMF as well, but due to the solar wind carrying the magnetic field and the winding of the magnetic field to a spiral, in the ecliptic plane the magnetic field strength goes $B \propto r^{-1}$ (Koskinen, 2011). Far northward and southward of the ecliptic plane and the HCS, the IMF indeed falls inversely to the square of the distance, as it normally does.

Stream interaction regions (SIRs) are known to be driving forces behind geomagnetic storms (Koskinen, 2011; Richardson, 2018). A stream interaction region forms when fast solar wind originating from a coronal hole overtakes the slow solar wind preceding it. Coronal holes tend to persist for several months at a time and

for this reason a new SIR originating from the same coronal hole may sweep past the Earth multiple times. There is a ~ 27 day period in the rotation of the Sun in the low latitudes and consequently there is the same period in SIRs from the same coronal hole, which is why they are often interchangeably referred to as *corotating interaction regions* (CIRs). In the CIR region the flow of plasma is fast compared to the ambient. This leads to the solar wind plasma being compressed in the CIR region, thus increasing the density of plasma. Since the magnetic field is frozen in to the fast flowing plasma, so too does the magnitude of IMF get stronger in the CIR region (Richardson, 2018). For these reasons the front of a CIR will eventually turn into a shock, though most often this happens at a distance larger than 1 AU ($\approx 150 \cdot 10^6$ km) from the Sun. It is usually not the shock itself, but the fast flow of plasma following the forming shock front that in conjunction with a favorably aligned IMF that triggers and drives a geomagnetic storm (Koskinen, 2011).

Geomagnetic storms are periods of time when the magnetic field of Earth is disrupted (Gonzalez et al., 1994). The effects of such storms can extend from increasing fluxes of high-energy plasma flows around the Earth, to inducing currents to human built infrastructure, such as electric power transmission grids (Pirjola, 2000). The increased fluxes of highly energetic particles can be dangerous to technological equipment in space, such as satellites and human life in orbit. Electric currents induced by magnetic storms on the other hand are known to be able to break electrical infrastructure on the surface of the Earth. Such an occurrence is, for example, the famous March 1989 geomagnetic storm, which caused a massive 12-hour blackout in the whole Canadian province of Quebec.

In this thesis, we study a set of observed geomagnetic storms, which are driven by high speed solar wind streams. In particular, we study the effects these storms had on the regions called the Van Allen belts and the high-energy electrons that reside within them.

2 Background

In this section we will go through the necessary theory, processes, and coordinate systems to lay foundation for the study conducted in this thesis. We start by introducing the relevant coordinate systems, from which we move on to describe the magnetosphere of the Earth. We then discuss what are the radiation belts and how do geomagnetic storms affect them.

2.1 Coordinate Systems

There is no single coordinate system that would be reasonable for all scales and processes. For this reason, we use different coordinate systems, e.g. for the IMF and for the particle fluxes around the Earth. In this chapter, we present the coordinate systems that are necessary for the work done in this thesis.

2.1.1 GSE and GSM coordinates

Geocentric Solar Ecliptic coordinate system (GSE) is a widely-used choice of coordinates when operating in near-Earth interplanetary space. It is defined as follows: X_{GSE} points from the center of the Earth to the center of the Sun. Y_{GSE} lies in the ecliptic plane, which is the plane in which Earth orbits the Sun, pointing against the direction of Earth's orbital motion. Finally, Z_{GSE} completes the right-handed coordinate system, aligned with the northward normal of the ecliptic plane. In the Geocentric Solar Magnetospheric coordinate system (GSM) the X_{GSM} axis is completely identical to the GSE coordinate system. Y_{GSM} is perpendicular to both X_{GSM} and the magnetic dipole of the Earth, pointing in the dusk side of the Earth. Z_{GSM} then completes the right-handed coordinate system such that Earth's magnetic dipole stays in the XZ-plane. More information about near-Earth space coordinate systems can be found, e.g. from the comprehensive review paper by Laundal and Richmond (2017). In this thesis, we employ GSE and GSM coordinate

systems to present data from interplanetary space in front of Earth's magnetosphere, e.g. the direction of IMF.

2.1.2 The McIlwain L-parameter

The L-parameter is a widely used coordinate in magnetospheric research. It was defined by McIlwain (1961) as a function of magnetic field B and an adiabatic invariant I, to organize measurements done of magnetically trapped particles at different geographic locations.

We can write the L-parameter as

$$L = \frac{r_0}{R_E}, \tag{1}$$

where r_0 is the distance from the axis of the dipole to the point at which the magnetic field line crosses the magnetic equator, and $R_E \approx 6370$ km is the radius of the Earth. Hence, we can think a certain L-value as being the set of all magnetic field lines, which cross the magnetic equator at a specific distance from the Earth. Using the L-parameter we can find an equation for a field line in units of Earth radii:

$$r = L\cos^2(\lambda), \tag{2}$$

where r traces the field line and λ is the magnetic latitude. Even though the magnetic field of Earth is most certainly not really a dipole field, it is reasonably well approximated as such in the range from roughly 2-7 R_E from the Earth's center, as stated for example in the textbook by Kilpua and Koskinen (2017). This range also happens to include vast majority of the Van Allen belts, which is also why it is extremely useful coordinate for studying them.

2.2 The Magnetosphere

Earth gets its magnetic field from the molten core of iron deep in the planet's center, acting as a dynamo. This geomagnetic field reaches far into space, getting

gradually weaker as distance grows. The magnetosphere is the region of space, that is dominated by the influence of the geomagnetic field of the Earth. Viewed from a distance, Earth's magnetic field closely resembles that of a dipole magnet. The magnetosphere is not a symmetric bubble, but is instead pushed in from the day side of the Earth and elongated to a long tail in the night side by the solar wind. Figure 1 shows a schematic picture of the magnetosphere.

Solar wind is fast flowing plasma and it carries the Sun's magnetic field within it. This is due to the frozen-in condition of plasmas. When the dynamic pressure of plasma is large in comparison to the magnetic pressure, two elements of plasma inhabiting the same magnetic field line will stay on the same field line. This makes it appear as if the plasma is carrying the magnetic field lines within it. For this reason different populations of plasmas will not mix together. Instead, a rather distinct boundary layer called *magnetopause* forms between the solar wind plasma and magnetospheric plasma.

Magnetopause is not by any means a rigid surface but instead a rather dynamic boundary which depends largely on the circumstances in the local interplanetary space. In this thesis, we employ a commonly used model for the shape and size of the magnetopause (Shue, 1997):

$$r = r_0 \left(\frac{2}{1 + \cos(\theta)} \right)^{\alpha}, \tag{3}$$

where r is the radial distance between the center of the Earth and magnetopause, and θ is the angle between the radial direction and the Sun-Earth line. r_0 is called the standoff distance and α is the level of tail flaring. They are calculated separately as follows:

$$r_0 = \begin{cases} (11.4 + 0.013B_z)D_p^{-\frac{1}{6.6}}, & \text{for } B_z \geq 0 \\ (11.4 + 0.14B_z)D_p^{-\frac{1}{6.6}}, & \text{for } B_z < 0 \end{cases}$$

$$\alpha = (0.58 - 0.010B_z)(1 + 0.010D_p),$$

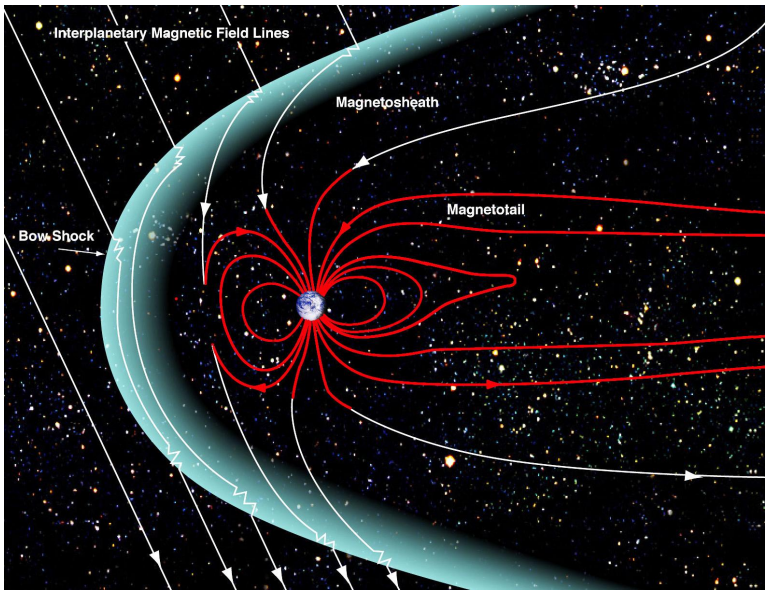

Figure 1. A schematic picture of the magnetosphere. Solar wind pushes the dayside of magnetosphere inward and elongates the nightside outward to a long magnetotail. A supersonic shockwave forms in front of the magnetosphere, called the bow shock. The turbulent region between bow shock and magnetopause is called the magnetosheath. Credit: (*NASA/Goddard/Aaron Kaase*, 2017)

where B_z is the z-component of IMF and D_p is the dynamic pressure of the solar wind plasma. This model was developed in a study by Shue (1997) and further tested under extreme solar wind conditions by Shue et al. (1998).

Because the flow of solar wind at 1 AU is supermagnetosonic, which means that the flow itself is faster than the propagation of information within the medium by mechanical or magnetosonic waves, there forms a shock in front of the magnetopause. The shock is quite analogous to a shock forming in front of, for example, a supersonic aircraft. This shock is called the bow shock, and the region of space between the bow shock and magnetopause is called magnetosheath. Crossing the bow shock transforms great amounts of energy from kinetic energy to heat and electromagnetic energy, which is why in the magnetosheath the flow of plasma has become slow and turbulent, compared to the ambient solar wind flow. Not all of the incoming solar wind will cross the shock, instead a portion is reflected and deflected. The position

of the nose of the bow shock, as well as the overall shape, depends on a variety of parameters, such as the dynamic pressure of the solar wind and the strength of IMF. A frequently used three-dimensional parabolic model for mapping the position of the bow shock was derived by Peredo et al. (1995), utilizing magnetohydrodynamic equations and upstream Alfvénic mach numbers. This model was since further improved by Merka et al. (2005), where they derived two models for the expected position and shape of the bow shock in two widely-used space coordinate systems.

2.3 The Radiation Belts

The radiation belts, also known as Van Allen belts, are torus-shaped shells of energetic plasma flowing around the Earth. The radiation belts overlap with another structure relevant to this thesis, which is the *ring current* (RC). Together these structures form the region of space called plasmasphere. To understand how these structures are formed and why do they exist we will now go through the relevant steps using the physical theory of charged particles in electromagnetic fields. The equation of motion for a charged particle is:

$$m\frac{d\mathbf{v}}{dt} = q(\mathbf{E} + \mathbf{v} \times \mathbf{B}) + \mathbf{F}_{non-EM}, \tag{4}$$

where m and q are the mass and charge of the particle, $\mathbf{v}$ is the velocity of the particle, $\mathbf{E}$ is the electric field, $\mathbf{B}$ is the magnetic field, and $\mathbf{F}_{non-EM}$ are all the non-electromagnetic forces. It is helpful to make some justified approximations that usually apply to the near-Earth magnetospheric regime, such as neglecting gravity and electric field. In such case, the magnetic field is the only one exerting force on the particle. From the resulting form one reaches an equation of motion that predicts a constant linear motion parallel to the magnetic field ($v_{\|}$ =constant) and circular motion on a plane which is perpendicular to the direction of that field. Such

a trajectory is called a helix, and the pitch angle of this helix is:

$$\tan(\alpha) = \frac{v_\perp}{v_\parallel}$$
$$\rightarrow \alpha = \arcsin(\frac{v_\perp}{v}), \tag{5}$$

where $v_\perp = \sqrt{v_x^2 + v_y^2}$ is the particle's velocity component perpendicular to $\mathbf{B}$. Thus, pitch angle simply means the angle between the parallel and perpendicular components of the particle's velocity. The radius of this circular motion is called the Larmor radius or the gyroradius:

$$r_L = \frac{mv_\perp}{|q|B}. \tag{6}$$

The center of the Larmor radius is called the *guiding center* (GC) and it follows the topology of the magnetic field, as long as the field varies slowly enough in space and time. Indeed, if the variations in the magnetic field emerge at scales larger than the Larmor scale, be that the spatial size of the radius or the timescale of the periodic motion, then there is a conserved quantity called the magnetic moment:

$$\mu = \frac{W_\perp}{B}, \tag{7}$$

where $W_\perp$ is the amount of kinetic energy associated with motion perpendicular to the magnetic field. The magnetic moment, when conserved, is called the *first adiabatic invariant* in plasma physics. In classical mechanics, an adiabatic invariant is a quantity that in periodic motion stays constant when the system around it changes slowly enough in time or space. For a proof of this, the reader is advised to see, for example, a classical mechanics textbook by Goldstein (1980).

One can see that if the particle's GC would move along a magnetic field line, which leads to a gradually stronger field, then in order conserve magnetic moment, so too must $W_\perp$ grow larger. Now, if we still insist that all other forces are negligible compared to the grip of the magnetic field, then the perpendicular kinetic energy $W_\perp$ must come from kinetic energy associated with the parallel motion $W_\parallel$. This leads

to the inevitable conclusion that the pitch angle α of the GC must tend towards a right angle when the magnetic field gets stronger. When the pitch angle of the particle reaches zero, the particle's motion along the field line briefly comes to a halt at the *mirroring point*. Now, since a gradient in the magnetic field will exert a force on a charged particle, such that (Kilpua and Koskinen, 2017):

$$\mathbf{F} = -\mu \nabla B, \tag{8}$$

where $\mathbf{F}$ is the force caused by the magnetic field gradient, the particle will be pushed back towards weaker magnetic field. In the case of the pitch angle of the GC becoming zero, it follows directly from Eq. (8) that the acceleration of the particle parallel to the magnetic field will be:

$$\frac{d\mathbf{v}_{\parallel}}{dt} = -\frac{\mu}{m} \nabla_{\parallel} B, \tag{9}$$

where $\mathbf{v}_{\parallel}$ and $\nabla_{\parallel}$ are the velocity and the gradient in the parallel direction of the magnetic field. This whole process of stopping and changing direction due to magnetic field gradient is called magnetic mirroring, and it is one of the reasons there are charged particles trapped in the magnetic field of the Earth. More information and examples of magnetic mirrors can be found from, e.g. the textbook by Kilpua and Koskinen (2017).

Particles trapped in the geomagnetic field will achieve their maximum pitch angle in the magnetic equator. Naturally there will be a distribution of different pitch angles, and some of the pitch angles will be close enough to a right angle that those particles never leave far from the magnetic equator before mirroring back. On the opposite side of the distribution are the particles with pitch angles so small that the mirroring point lies somewhere in the atmosphere or even inside the Earth. These particles will not bounce back, but instead precipitate into the atmosphere where they will eventually collide with some molecule, thus ionizing it and becoming part of the atmosphere. They will be lost from the radiation belts altogether and we say they are in the "bounce loss cone" of the pitch angle distribution.

As stated before, a gradient in the magnetic field will exert a force on a charged particle. In the geomagnetic field, there is a gradient in the strength of the field, but also in the curvature of the field. Because of the force exerted by the gradient and the curvature, charged particles will also drift around the Earth. In total there are three periodical motions for the particles that are trapped in the geomagnetic field. These are the gyration around a magnetic field line, bouncing between two magnetic mirroring points, and the gradient-curvature drift around the Earth. It is important to make a distinction here between the bounce loss cone and drift loss cone. As mentioned, bounce loss cone includes all particles with a small enough pitch angle for the particle to precipitate into the atmosphere and be erased from the radiation belts. By drift loss cone we mean those particles that in their current longitude could bounce between north and south ad infinitum, but because of their drift around the Earth due to gradient and curvature of the magnetic field end up on longitudes where their new mirroring point ends up inside the atmosphere or lower. Mirroring point depends also on the magnetic longitude a particle is on because Earth's dipole field is both tilted and spatially offset from Earth's rotational axis.

2.3.1 History

The first major discovery of the Space Age could very well be attributed to the founding of the radiation belts by Geiger counters aboard the Explorer-1 rocket in 1958, which was originally designed to study cosmic rays entering Earth's atmosphere (Van Allen et al., 1958). The particle fluxes far exceeded the expectations based on earlier cosmic ray measurements, causing dead-time saturation of the instruments on Explorer-1. The cause of the saturation of the Geiger counters was then identified as high fluxes of magnetically trapped particles in a low-altitude zone of the inner radiation belts.

2.3.2 The Inner and Outer Belt

The inner radiation belt extend from L-values of 1 to roughly 3. The particle population trapped in this region consists of mainly energetic ions with energy exceeding 100 MeV and electrons in the range of some hundreds of keVs (Li and Hudson, 2019). Electrons actually have a two-belt structure, but ions in the range of MeVs are only confined to the inner belt. This is because the geomagnetic field further away from the Earth is too weak to keep ions in tight enough grip to keep them trapped. The Larmor radius of MeV ions becomes comparable to the local magnetic field gradient at an altitude of $\sim 2\ R_E$ in the equatorial plane. As was stated in section 2.3, if the magnetic field changes faster than the particle gyrates, then magnetic moment is not conserved anymore. If magnetic moment is not conserved, the particle is no longer bound to the field and thus is able to escape. The two-belt structure of the radiation belts is illustrated in Fig. 2.

The protons of the inner belt come mainly from cosmic ray particles interacting with the upper atmosphere, the phenomenon is known as Cosmic Ray Albedo Neutron Decay (CRAND). Cosmic rays are high-energy particles, usually ions, which have been accelerated to effectively the speed of light, by scattering for millions of years in the galactic magnetic field. The injection of a cosmic ray particle into the atmosphere may produce a shower of secondary particles, such as muons. It may also produce neutrons that decay in roughly 15 minutes into a proton and an electron. The electron population in the inner belt is refreshed periodically by outer belt electrons being transported inward in slot-penetrating events. Solar energetic particles (SEPs) accelerated by energetic events from the Sun, such as CMEs, are also known to become trapped in the inner radiation belt (Li and Hudson, 2019). Due to the tilt and offset of the Earth's magnetic axis in relation to it's spin axis, it follows that the inner radiation belt comes particularly near the Earth's surface at a specific region. This region is known as the South Atlantic Anomaly (SAA), since

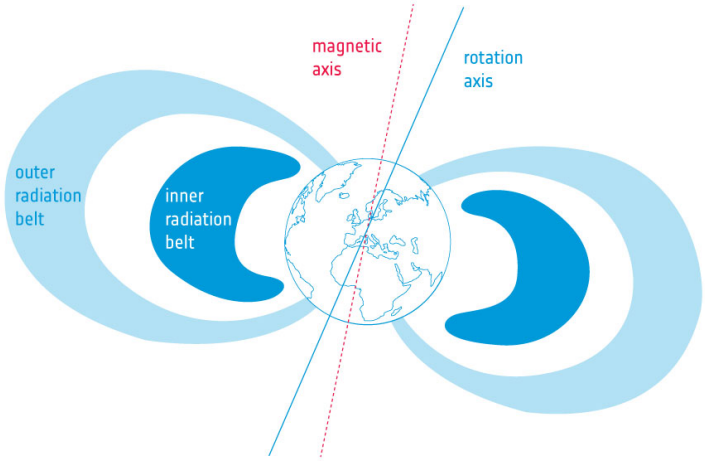

Figure 2. An illustrative picture showing the inner and outer radiation belts in relation to the Earth's rotational spin axis and the magnetic dipole axis. Credit: The European Space Agency, (*ESA/Image Gallery*, 2016)

the particle fluxes in that geographic region are anomalously high at low altitudes.

The outer radiation belt consists of mainly energetic electrons in the range from 0.1 MeV to 10 MeV, many of which are accelerated by different processes to ultrarelativistic energies. A particle is called ultrarelativistic when its kinetic energy becomes comparable to the energy associated with its mass. The extent of the outer belt is a little difficult to exactly state due to its more variable nature, but a range of roughly $3 < L < 7$ is usually agreed on (Millan and Thorne, 2007; Bingham et al., 2018; Turner et al., 2019). The outer belt is known to be much less stable in its structure than the inner belt (Millan and Thorne, 2007). This has to do with the different source and loss processes of the inner belt ions and lower energy electrons, compared to the higher energy electrons of the outer belt. Electrons are known to drop from outer L-shells into lower ones due to radial diffusion. This can lead to acceleration due to the conservation of magnetic moment μ (Millan and Thorne, 2007). Another process which erases electrons from the outer belt is scattering due to whistler waves (Lyons and Thorne, 1973; Millan and Thorne, 2007).

2.4 Geomagnetic Storms

Geomagnetic storms, also called magnetospheric storms, are temporary disturbances in Earth's magnetic field. In more technical terms, they are defined by Gonzalez et al. (1994) as periods of time when the flow of energy from the interplanetary space in to the magnetosphere causes the magnetospheric ring current to intensify in a sufficient amount, that the resulting induced magnetic field that opposes that of Earth's exceeds a specific threshold. Geomagnetic storms typically last from hours to even days, and it's possible for the next storm to begin before the previous one has passed.

Geomagnetic storms are most often initiated by interplanetary coronal mass ejection (ICME) driven shocks and fast solar wind streams coming after a CIR passes. Storms driven by fast solar wind streams are often classified as recurrent storms, since they reappear periodically. This is due to the same coronal hole facing Earth as the Sun rotates, and as we have stated earlier, fast solar wind in the ecliptic plane originates from coronal holes. We will take a closer look at storms driven by fast solar wind flows later in this chapter, since they play a central role in the subject of this thesis. The strongest geomagnetic storms are usually the ones driven by ICMEs (Koskinen, 2011).

2.4.1 Magnetospheric Storms and Substorms

As discussed earlier, magnetospheric storms are periods of time when the geomagnetic field is strongly disturbed. An exact definition of what qualifies as "strong perturbation" is of course somewhat arbitrary and depends on what is generally agreed as a threshold. A convention adopted by many is to classify storms yielding a *Disturbance storm time* (Dst) index of -30 nT to -50 nT as *small*, from -50 nT to -100 nT as *moderate*, and from -100 nT onward as *intense* (Gonzalez et al., 1994). These are also the thresholds we have chosen to use to identify time periods

of magnetospheric storms.

Dst index is calculated as the weighted average of the deviations from the normal horizontal components of the magnetic field, measured in four different low-latitude stations around the Earth. Thus, *Dst* is a measure of how much the ring current weakens the geomagnetic field. There exists other metrics for measuring the strength of magnetic storms as well, such as the *Auroral Electrojet* (*AE*) index, K_{p} index, and Dst^{*}, which is the pressure-corrected *Dst* index. In this work we limit the analysis to the regular *Dst* and sometimes for the *AE* as well for reference. AE index is a measure of the global electrojet activity in the auroral zone of the Earth. It's calculated using geomagnetic field measurements from twelve stations in the northern hemisphere auroral zone. More information about *Dst* and the other indices mentioned can be found in the textbook by Koskinen (2011).

Different storm phases can be identified from the temporal evolution of the *Dst* index. It is not uncommon that prior to the commencement of a magnetic storm, there is a brief (positive) increase in the *Dst* index. It is especially the case with an ICME-driven storm that there would be a noticeable positive "bump" in the *Dst* before the decline towards peak minimum *Dst* begins. This positive deviation is a signature of the magnetopause being pushed in closer to the Earth, thus amplifying the Chapman-Ferraro current ($\mathbf{J}_{CF}$ flows eastward on the dayside; opposite to the RC) that induces a magnetic field, which aligns with the geomagnetic field (Koskinen, 2011). The brief *initial phase* is followed by a rapid decline in the *Dst* index towards the peak minimum. This is the *main phase* of a geomagnetic storm, during which the ring current is enhanced by the inflowing energy and particles from the solar wind outside the magnetosphere. The transition from the initial phase to the main phase strongly depends on the configuration of the IMF. With consistent southward IMF from the start of the contact with the storm's driver, the initial phase may be very brief. This is because the flow of energy into the magnetosphere

becomes immediately accessible, thus quickly commencing the main phase. However, if the IMF is directed northward, then the main phase will not commence until the IMF turns southward to enable enhanced magnetic reconnection on the dayside of the magnetopause. When the flow of energy and particles into the magnetosphere inevitably diminishes as the storm driver passes, so too does the ring current begin to lose the net energy it gained. This in turn leads to the *Dst* index slowly returning to the background level, marking the end of the main phase and the start of *recovery phase*. The recovery phase is usually longer than the main phase because the loss of current carriers and energy from the ring current is not as explosive effect as enhancement is (Koskinen, 2011; Kamide et al., 1998).

One of the main effects that characterize a period of a geomagnetic storm is the enhancement of the ring current. The ring current's main part is flowing at roughly 3 to 4 Earth radii from planetary center near the equatorial plane. It mainly consists of protons and O^+ ions, but also of electrons mainly in the 10-300 keV range, according to Gonzalez et al. (1994). The direction of this current is, when looking down from the north, clockwise. Hence, as stated by Ampere's law

$$\nabla \times \mathbf{B} = \mu_0 \mathbf{J}, \tag{10}$$

where μ_0 is the permeability of free space and $\mathbf{J}$ is current density, the ring current induces a magnetic field that opposes the geomagnetic field at the equatorial plane. Enhancement in the ring current therefore causes weakened geomagnetic field, which means that the magnetopause can be more easily pushed closer to Earth by the solar wind. The most immediate particle sources for the ring current are the magnetospheric plasma sheet in the magnetotail and the terrestrial ionosphere. Since the plasma sheet's particle population comes from the solar wind and the ionosphere, it also acts as a mediator of solar wind particles to the ring current (Daglis et al., 1999).

The overall strength of the RC is ultimately dependent upon the balance between

loss and injection of current carriers. The ring current is constantly losing particles, but the injection of new particles during the main phase of a storm dominates over the loss processes, thus resulting in increasing net current. Ions are the more important of the current carriers in the RC, and they are mainly lost by a process called *charge exchange*. Charge exchange is usually a collision between a neutral atom and an ion, in which the atom essentially donates an electron to the ion. A simple case of charge exchange can be mathematically formulated as follows (Koskinen, 2011):

$$X^{n+} + Y \rightarrow X^{(n-1)+} + Y^{+}$$

where X is the ion, Y is the originally neutral atom, and n is a natural number. In the ring current charge exchanges happen mostly between ions of the RC and neutral hydrogen of the extension of Earth's exosphere, also called the *geocorona*, which is relatively cold compared to the RC, thus transferring charge from fast carriers to very inefficient carriers. Another important process, which removes current carriers from the RC, is pitch angle scattering of the particles into the atmospheric loss cone. This process acts on electrons as well. The driving forces of pitch angle scattering in the RC are mainly Coulomb collisions and wave-particle interactions (Koskinen, 2011).

The reach of a magnetospheric storm is indeed global. However, many much more localized substorms may occur during a global geomagnetic storm. Substorms are not, despite their suggestive name, some little storms which together sum up to a magnetospheric storm. Instead, substorms can take place in times when there is no magnetospheric storm, and non-storm-time substorms are actually even more common than those happening during great magnetospheric storms. In his paper Akasofu (1964) found that isolated substorms have two characteristic phases, which are the expansive and recovery phase. Each phase can further be divided into three distinct stages. Substorm events last typically from 2 to 4 hours, and they are known

to inject particles into the inner magnetosphere (Koskinen, 2011).

2.4.2 Storms Driven by Fast Solar Wind Flows

Considering the heliosphere as a whole, fast solar wind is overwhelmingly more common than slow solar wind. Slow solar wind is strongly restricted to the vicinity of the heliospheric current sheet due to its origin being the streamers near Sun's equator, while fast wind flows out from the open field lines at higher latitudes and coronal holes. Earth's orbit lies in a region which is most of the time under slow solar wind's influence and periods of fast solar wind flows are not that common.

A corotating interaction region is formed when fast solar wind overtakes slow solar wind and this interface region will eventually turn into a shock. This usually happens at a distance greater than Earth's orbit (1 AU) though. If the alignment of the IMF is southward during the passing of a CIR, then that is to be taken as a warning of upcoming enhanced magnetospheric activity. This is why storms driven by fast solar wind are often interchangeably called CIR-driven storms, even though the driver of the storm is most often not actually the CIR itself, but the fast solar wind coming after it.

There is a rather strong periodicity with CIR-driven storms. It is approximately 27 days that it takes for a coronal hole near the solar ecliptic to make a full round around the Sun, and this is consequently also the length of the period between recurring CIR-driven storms. However, this does not necessarily apply to all times, since large coronal holes near the ecliptic (which is to say in low latitudes) mostly appear only during the declining phase of a solar cycle. Some fast solar wind periods do occur also independently from the recurrent ones, but they are usually weaker and do not last as long (Koskinen, 2011).

Even though storms driven by fast solar wind may not cause such high peak Dst values as ICME-driven storms, their cumulative effects can nevertheless be-

come more severe than with their ICME-driven counterparts. This is because CIRs usually form in regions where the Z-component of the IMF changes direction. So for example, if the IMF is oriented southward in the flow of the fast wind (which is a necessity for a magnetic storm), then it probably was oriented northward in the preceding flow of slow solar wind. Due to the southward pointing IMF in the flow of fast solar wind potentially lasting much longer than the relatively sudden passing of an ICME, the overall flow of energy into the magnetosphere can over time grow larger than with an ICME-driven storm. CIR-driven storms thus usually last longer and can over time become more severe than ICME-driven storms. It is known that storms driven by fast solar wind may produce larger fluxes of relativistic electrons in the inner magnetosphere than ICME-driven storms (Koskinen, 2011).

2.4.3 Effects on the Radiation Belts

Each magnetic storm is different, and trying to predict the specific effects of a storm beforehand is an extremely challenging endeavor. Regarding the radiation belt dynamics, they could enhance, deplete, or not really affect the belts. Storms affect ions and electrons differently, and the effects are different depending on the energies of the particles and the L-shells they inhabit. The outer belt electron structure is known to be highly dynamic during storm time, with trapped fluxes varying by over two orders of magnitude in a matter of hours (Millan and Thorne, 2007).

A large study on relativistic electrons and their responses to 276 geomagnetic storms was conducted by Reeves et al. (2003), with a dataset temporally spanning over 11 years from 1989 to 2000. They restricted the dataset to only moderate and intense geomagnetic storms, and found that 53 % of the storms enhanced the fluxes of relativistic electrons, 19 % of the storms decreased fluxes, and 28 % did not noticeably affect the fluxes. They also found that higher solar wind speed correlated

with the probability of higher flux increase.

Turner et al. (2015) studied 52 geomagnetic storms using data from the MagEIS instrument of the Van Allen Probes and found that storm time electron responses are highly dependent on the energy and L-shell of the electron. Their dataset included electrons with energies ranging from tens of keV to 2 MeV and L-values from 2.5 to 6.0. They found that enhancement events are the most common with over 50 % of the cases for energies with $E < 100$ keV in the majority of outer belt region, while depletion events for the same populations happened in less than 22 % of the storms.

A relatively recent study by Bingham et al. (2018) examined the local acceleration of subrelativistic electrons to relativistic speeds via wave-particle interaction in magnetospheric storms driven by CMEs and CIRs. They too used electron data from MagEIS on board the Van Allen Probes to study 25 CME-driven and 35 CIR-driven storms. They found that on average, CMEs enhance electron fluxes from lower L-values to higher fluxes and faster than CIR-driven storms.

There is also some dependence on the energies of the electrons to the losses on the shells. Horne et al. (2009) concluded that outer radiation belt electron precipitation happens mostly during the main phase for $E > 300$ keV electrons, while $E > 1$ MeV electron precipitation peaks during the recovery phase. Precipitation in this context means that the electrons' magnetic mirroring point is at such a low altitude that they "rain down" into the atmosphere, thus being lost from the radiation belts. Their more than 9 years spanning dataset suggested that the lower energy electrons were more likely to be precipitated due to belonging to the bounce loss cone, whereas the higher energies were more likely lost into the drift loss cone. This study was, however, limited to only include storms stronger than $Dst < -70$ nT.

3 Data Analysis and Methods

In this work we use observational data from three separate space missions: Aalto-1, PROBA-V, and the Van Allen Probes, which we will present in this chapter. We go through the very main points of each mission and take a closer look at the relevant instruments that have recorded the data we use in this study. We then describe in detail the methods of analysis and the motivation behind them.

3.1 Data

For all data measured by Aalto-1/RADMON and PROBA-V/EPT, we used a dataset compiled by Gieseler et al. (2019) for the study of the first results produced by RADMON (Gieseler et al., 2020). This dataset temporally covers the months from October to December in 2017. The corresponding dataset for measurements done by Van Allen Probes was downloaded from *RBSP-ECT Science and Data Portal* (n.d.).

The dataset for interplanetary conditions was acquired from NASA Coordinated Data Analysis Web (King and Papitashvili, 2005). The dataset contains magnetic field, solar wind, and AE index data with one minute resolution. The Dst index has a resolution of one hour. Dst and AE indices in the dataset come from the World Data Center for Geomagnetism, Kyoto (*Geomagnetic Dst index*, 2015), (*Geomagnetic AE index*, 2015).

3.2 Space Missions and Instruments

We employed three separate space missions for the analysis done in this work. In this chapter we present these missions and their relevant instruments.

3.2.1 Aalto-1 and RADMON

Aalto-1 (Kestilä et al., 2013; Praks et al., 2021; Mughal et al., 2021) is a Finnish nanosatellite, launched on 2017-6-23 to an sun-synchronous polar orbit, with an orbital inclination of 97.4°. A Sun-synchronous orbit (SSO) is such that the satellite passes through the same point relative to the Sun each orbit, and a polar orbit means that the satellite traverses over Earth's poles every orbit. Aalto-1's orbit is a Low Earth Orbit (LEO), with a mean altitude of a little over 500 km. With a mass of only 4 kg, Aalto-1 is carrying three main payloads: a spectral imager, a particle telescope, and a plasma brake. The main interest in this thesis is on the particle telescope, RADMON (Peltonen et al., 2014; Oleynik et al., 2020).

RADMON (Radiation Monitor) is an energetic particle monitor, developed in collaboration with Finnish university students for the Aalto-1 mission. It consists of two silicon detectors and a CsI-scintillator, and utilizes the ΔE-E method to determine particle energy and species. RADMON detects protons and electrons in integral channels. This means that for a given channel, e.g. e2, which is an electron channel, all electrons with an energy of more than 1.5 MeV are measured. The different RADMON energy channels and explanations are presented in table I. It has been demonstrated by Gieseler et al. (2020) that RADMON is capable of observing energetic electrons in integral intensities above 1.5 MeV. RADMON counts the amount of particles that come in to the detector over an interval of 15 seconds. These counts then have to be transformed into the physical quantity of intensity.

3.2.2 PROBA-V and EPT

PROBA-V (Project for On-Board Autonomy–Vegetation) is an ESA-operated satellite and a part of the larger PROBA program. It was built in Belgium and launched to a sun-synchronous polar LEO on 2013-5-7. PROBA-V orbits at an altitude of

Channel	Primary species	Contaminating species	Units
e2	$>$ 1.5 MeV electron	$>$ 100 MeV proton	$(\mathrm{cm}^2\ \mathrm{sr}\ \mathrm{s})^{-1}$
e3	$>$ 3.1 MeV electron	$>$ 80 MeV proton	$(\mathrm{cm}^2\ \mathrm{sr}\ \mathrm{s})^{-1}$
e4	$>$ 6.0 MeV electron	$>$ 70 MeV proton	$(\mathrm{cm}^2\ \mathrm{sr}\ \mathrm{s})^{-1}$
i1	$>$ 10.4 MeV proton	-	$(\mathrm{cm}^2\ \mathrm{sr}\ \mathrm{s})^{-1}$
i2	$>$ 18.5 MeV proton	-	$(\mathrm{cm}^2\ \mathrm{sr}\ \mathrm{s})^{-1}$
i3	$>$ 23.7 MeV proton	-	$(\mathrm{cm}^2\ \mathrm{sr}\ \mathrm{s})^{-1}$
i4	$>$ 29 MeV proton	-	$(\mathrm{cm}^2\ \mathrm{sr}\ \mathrm{s})^{-1}$
i5	40–80 MeV proton	-	$(\mathrm{cm}^2\ \mathrm{sr}\ \mathrm{s}\ \mathrm{MeV})^{-1}$

Table I. RADMON energy channels included in the dataset by Gieseler et al. (2019). The electron channels e2, e3, and e4 are provided directly from the measurements. The proton channels through i1 to i5 are calculated as sums of the measured proton channels, such that i1 is the sum of channels p1 to p9, i2 is the sum of channels p2 to p9 etc. The response functions of RADMON can be found in Oleynik et al. (2020).

820 km, with an orbital inclination of 98.73°, and an orbital period of 101.21 minutes. It has a mass of 160 kg and carries two main payloads, which are a camera that is dedicated to monitoring Earth's vegetation and EPT (Energetic Particle Telescope). PROBA-V also carries other instruments aboard, but as with Aalto-1, the most relevant instrument for us in this study is EPT. More information about PROBA-V and the other PROBA missions is available at the *ESA Proba Missions* (n.d.) website.

EPT is a spectrometer specifically designed for measuring charged particle environments in space with high resolution (Cyamukungu et al., 2014). The EPT instrument is divided into two energy sections. The low energy section that consists of two silicon detectors employs the classical ΔE-E particle telescope method for detecting particle species and energy. The high energy section is further divided into 10 Digital and Absorber Modules (DAM), which are comprised of a silicon sensor and a sheet of absorber material. The time resolution of EPT is

Channel	Electrons [MeV]	Protons [MeV]	Helium ions [MeV]
1	0.5–0.6	9.5–13	38–51
2	0.6–0.7	13–29	51–116
3	0.7–0.8	29–61	116–245
4	0.8–1	61–92	246–365
5	1–2.4	92–126	365–500
6	2.4–8	126–155	500–615
7	8–20	155–182	615–720
8		182–205	720–815
9		205–227	815–900
10		227–248	900–980
11		> 248	> 980

Table II. Energy ranges of each channel of the EPT instrument aboard PROBA-V. Source: Pierrard et al. (2014).

adjustable, but the default setting is 2 seconds, which means that the particles EPT counts are integrated over 2 seconds. The specific particle energies per EPT channel are presented in table II. Since particles detected by EPT are divided into channels of specific energy range, their flux is given in units of differential flux. This means that the observed flux has units of flux per energy.

3.2.3 Van Allen Probes and REPT

The Van Allen Probes mission, also known as the Radiation Belt Storm Probes (RBSP) mission, was a high profile NASA mission, consisting of two identical twin satellites. A direct quote from Mauk et al. (2013), explaining the fundamental science objective of the RBSP mission reads: "Provide understanding, ideally to the point of predictability, of how populations of relativistic electrons and penetrating ions in space form or change in response to variable inputs of energy from the Sun."

The twin probes were launched on 2012-8-30 and are on highly elliptic orbits (HEO), with perigee at ∼600 km altitude, apogee at ∼5.8 R_E, and orbital period of 9 hours. There is roughly a 160 km difference in the apogees of the two probes, causing one probe to lap the other every 75 days. Due to the low inclination of the orbits, the Van Allen Probes are limited in their scope of reachable L-values compared to Aalto-1 and PROBA-V. They do however venture much farther into the radiation belts, which means they are able to see much more of the particle populations on each L-shell. More detailed information about the RBSP mission is in the paper by Mauk et al. (2013).

Both RBSP carry identical instrumentation inside. The Energetic Particle, Composition, and Thermal Plasma (ECT) suite holds three highly coordinated instruments, which are the Magnetic Electron Ion Spectrometer (MagEIS), the Helium Oxygen Proton Electron (HOPE) sensor, and the Relativistic Electron Proton Telescope (REPT). All three of these instruments are particle detectors, but in this thesis we only examine data produced by REPT, since it is specifically designed for high-energy particle observations. Spence et al. (2013) describe the ECT suite in detail.

The REPT (Baker et al., 2013) is a high-performance particle telescope designed to withstand the high radiation environment of the outer radiation belt. It is capable of measuring particles of very high energy, and it consists of multiple Si solid-state detectors stacked on top of each other and a collimator. The employed ΔE-E method allows for 11 differential energy channels for electrons and 7 for protons, leaving the last ones to be measured as integral channels. See table III for a list of REPT energy channels per particle species. The whole instrument is encased in a thick aluminum case that shields the detectors from penetrating high-energy particles and an inner shield made out of tungsten-copper alloy to stop bremsstrahlung.

Channel	Electrons [MeV]	Protons [MeV]
1	1.6–2.0	18.5–24.0
2	2.0–2.5	24.0–31.2
3	2.5–3.2	31.2–40.6
4	3.2–4.0	40.6–52.8
5	4.0–5.0	52.6–68.6
6	5.0–6.2	68.6–89.2
7	6.2–7.7	89.2–116.0
8	7.7–9.7	$>$ 116.0
9	9.7–12.1	
10	12.1–15.1	
11	15.1–18.9	
12	$>$ 18.9	

Table III. Electron and proton energy bins of REPT aboard the Van Allen Probes. Source: Baker et al. (2013)

3.3 Methods

To examine the effects geomagnetic storms had on the radiation belts' electrons during the Oct–Dec 2017 period, the measured electron intensity is plotted against a variety of coordinates. We also derive some important parameters that describe the large-scale particle population. In the following sections we will discuss in detail the methods of analysis used in this thesis.

3.3.1 Multipanel Timeseries

The main tool to visualize specifically what's happening in the big picture is a stacked multipanel timeseries. In multipanel timeseries plots we will stack plots of various data on top of each other. The panels are all aligned so that they share the same x-axis, which is time. This allows for comparing processes and events

happening in different locations at the same times. It also helps to see potentially correlating variables.

In the first panel is plotted the strength of the IMF. We also average the B_z component over 30 minutes to smooth out the small scale turbulence. B_z is particularly interesting because during southward IMF ($B_z < 0$) there is an amplified chance for magnetic reconnection at the nose of the magnetopause. The second panel contains the speed and pressure of the solar wind. In the third panel we plot the Dst and AE indices. The Dst is used to identify geomagnetic storms, and AE index is known to be an indicator of substorm activity. We mark the thresholds for a small geomagnetic storm ($Dst < 30\,\mathrm{nT}$) and a moderate storm ($Dst < 50\,\mathrm{nT}$) on the plot as horizontal dotted lines. The data plotted in the first three panels is from the OMNI dataset. OMNI data shares the same time resolution of 60 seconds, except for the Dst index, which has a resolution of 60 minutes.

The next panels representing measurements done by the three space missions are all plotted according to the same methodology. The x-axis is still the same time period as it is for the OMNI data in the first three panels, and it is temporally aligned so that every panel shares the same x-axis. However, for the electron flux measurements we choose to employ a histogram-type of representation. The temporal resolution will be adjusted manually in each of these panels according to the presented time window. The y-axis is then chosen to show the L-parameter. Employing the same mechanism as we do with the x-axis, we discretize the y-axis to equally wide bins with a resolution of 0.25 L. We always begin the y-axis from an L-value of 1 and end in L-value of 10. As an example to the reader we present the whole length of the dataset with all measured values in Fig. 3.

When time- and L-axes are each divided into bins as described above, what we get is a 2-dimensional grid of rectangular bins in which to place the electron intensity measurements. We treat each bin as a semi-open interval, such that a measurement

taken at the starting point of a bin is put in to that bin. The bins have no values between them, instead the ending point of nth bin is also the starting point of $n+1$th bin. The electron intensity measurements are then mapped according to these rules into the bins. The value for each bin is then calculated as the arithmetic mean of all measurements in that specific bin. If there are no values in a bin, then the value for that bin is set to NaN, which means it's "Not a Number".

To represent the numerical value of a bin, we use as a foundation the jet.cm colormap provided by Python 3's Matplotlib library. In this colormap low values are colored blue and high values are colored red. The colormap is modified to show bins with a value of zero to be white, and bins with no measurements to be grey. The specific values each color corresponds to are displayed in the colorbars to the right of the panels.

3.3.2 Integration of Differential Intensity Measurements

In order to better compare the measurements done by RADMON aboard Aalto-1 and EPT aboard PROBA-V, we calculate an expected integrated electron intensity from EPT's differential intensity measurements. Our method for calculating integral intensity assumes that the electron flux being measured by the instrument follows a power law

$$j(E) = j_0 E^{-\gamma}, \tag{11}$$

where j is the intensity of particle flux in units of [cm^{-2} s^{-1} sr^{-1} MeV^{-1}], j_0 is a constant, E is the energy of an electron in MeVs, and γ is the spectral index. Integrating the flux of electrons over all energies above a certain threshold is done as follows:

$$J(> E_{\,\mathrm{th}}) = \int_{E_{\,\mathrm{th}}}^{\infty} j_0 E^{-\gamma}\,\mathrm{d}E = \frac{j_0}{\gamma - 1} E_{\,\mathrm{th}}^{1-\gamma}, \tag{12}$$

where $J(> E_{\,\mathrm{th}})$ is the integral intensity of particle flux in units of [cm^{-2} s^{-1} sr^{-1}] and $E_{\,\mathrm{th}}$ is the threshold energy from which onward all flux is measured. $E_{\,\mathrm{th}}$ is a

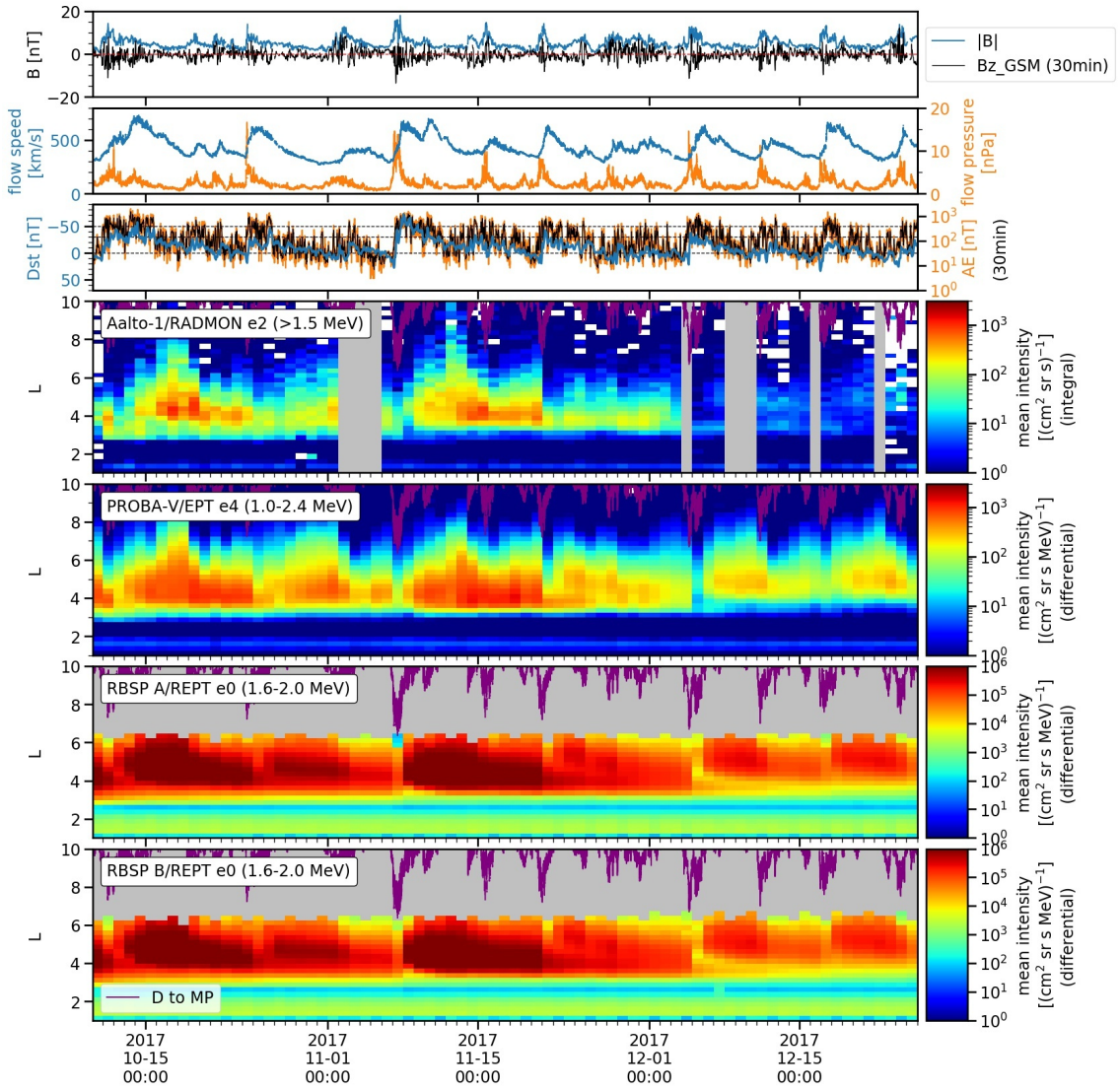

Figure 3. The stacked multipanel timeseries aligns data from different sources to a shared time window. The first two panels show the plasma parameters, which are the IMF and solar wind speed and pressure. The third panel shows the *Dst* and *AE* indices, which we use to identify geomagnetic storms. The rest of the panels show the daily average particle measurements by Aalto-1, PROBA-V, and the twin RBSP spacecraft as timeseries plotted against the L-parameter. The color coding of bins is presented to the right of each panel. White bins mean a zero measurement and grey bins are bad values or data gaps. The purple line going through all intensity plots is the daily average distance to the nose of the magnetopause, calculated as per Eq. (3). Here we display the whole period our dataset covers, from 2017-10-10 to 2017-12-26.

parameter we choose according to our needs, while j_0 and γ are free variables. For this, we need to use measurements from two separate channels. By knowing the intensity at two different energies, we can seek for a fit going through these intensity values and obtain j_0 and γ that describe the energy spectrum of the particles. We assumed that Eq. (11) holds for any differential channel measurement. It then follows that:

$$j_0 = j_i E_i^{\gamma} = j_{i+1} E_{i+1}^{\gamma} = \ ... \ = j_{i+n} E_{i+n}^{\gamma}, \tag{13}$$

where j_i and E_i are the intensity and energy of the ith channel, and n is a natural number. We cannot solve for j_0 without knowing γ, but we can use the chain of equalities in Eq. (13) to find an expression for γ such that:

$$\begin{aligned} j_i E_i^{\gamma} &= j_{i+1} E_{i+1}^{\gamma} \\ \rightarrow \left(\frac{E_i}{E_{i+1}}\right)^{\gamma} &= \frac{j_{i+1}}{j_i} \\ \rightarrow \gamma &= \frac{\ln(j_{i+1}) - \ln(j_i)}{\ln(E_i) - \ln(E_{i+1})} \end{aligned} \tag{14}$$

where ln() is the natural logarithm. One problem is, however, that no channel is infinitely thin, which means there is effectively an infinite amount of possible configurations for j_0 and γ for each pair of intensity measured in channels $j_i(E_i)$ and $j_{i+1}(E_{i+1})$. We overcome this problem by finding the effective energy E_{eff} for each of the two channels.

To find the effective energy of a specific channel, first consider that the instrument counts incoming particles in units of $[s^{-1}]$ as follows (Sullivan, 1971):

$$C_i = \int_0^{\infty} G_i(E) j(E) \, \mathrm{d}E = \int_{E_{i,1}}^{E_{i,2}} g_i j_0 E^{-\gamma} \, \mathrm{d}E, \tag{15}$$

where $E_{i,1}$ and $E_{i,2}$ are the upper and lower boundary of ith channel. We have also assumed that the geometric factor of the instrument in ith channel is $G_i = g_i$ and zero outside the channel's boundaries. This is not an obvious assumption and most

of the time not even completely true because a perfect ideal detector does not exist, but it is a reasonable approximation nonetheless.

The usual way to calculate intensity from counting rate in a differential channel is:

$$j_i = \frac{C_i}{g_i(E_{i,2} - E_{i,1})}. \tag{16}$$

By solving the integral in Eq. (15), we can express counts per second in terms of energy:

$$\int_{E_{i,1}}^{E_{i,2}} g_i j_0 E^{-\gamma} \, \mathrm{d}E = \frac{g_i j_0}{(-\gamma + 1)}(E_{i,2}^{-\gamma+1} - E_{i,1}^{-\gamma+1}).$$

Now, substituting this expression for C_i into Eq. (16) yields:

$$\begin{aligned} j_i &= \frac{C_i}{g_i(E_{i,2} - E_{i,1})} \\ \rightarrow j_0 E_{i,\,\mathrm{eff}}^{-\gamma} &= \frac{g_i j_0 (E_{i,2}^{-\gamma+1} - E_{i,1}^{-\gamma+1})}{g_i(-\gamma+1)(E_{i,2} - E_{i,1})} \\ \rightarrow E_{i,\,\mathrm{eff}} &= \left[\frac{(1-\gamma)(E_{i,2} - E_{i,1})}{(E_{i,2}^{1-\gamma} - E_{i,1}^{1-\gamma})}\right]^{1/\gamma}. \end{aligned}$$

As we can see, the effective energy of a channel is now only a function of the spectral index, since the channel boundaries are known constants. The problem is that we have no knowledge of γ beforehand. We can, however, guess what it could be and calculate the effective energy of two channels using this guess. We set our initial guess to $\gamma = 2$ and calculate the effective energy for two channels. Using the obtained values for $E_{i,\,\mathrm{eff}}$ and $E_{i+1,\,\mathrm{eff}}$, we then calculate a new value for γ using Eq. (14), which will be nearer the true value of γ. Using the calculated spectral index we again calculate new effective energies for both channels, which will be nearer the true effective energies. This iterative method is continued until the spectral index converges to its true value. Our numerical method stops the iteration process when the difference between two consecutive values for γ is less than 0.1.

Once the spectral index is solved, j_0 is found with a simple substitution of values to Eq. (13), from which the integral intensity J can be calculated with Eq. (12).

Figure 4 is an illustrative example of intensity measured by EPT from 2017-11-17 to 2017-11-19, averaged over time and L-values from 4.0 to 5.0. The plot shows the average differential intensity in each channel and a power-law fit through two channels. The plot also shows the calculated integral intensity profile and corresponding RADMON integral channels.

The integration method described in this section is individually applied to each bin of the grid in the stacked multipanel plots, presented in the section 3.3.1. Figure 5 presents a low-resolution comparison of RADMON and integrated EPT measurements, stacked in a multipanel timeseries.

3.3.3 Plotting Intensity as a Function of MLT

In order to better examine a periodical pattern of high intensities found in RADMON measurements, we plot time-averaged intensity histogram against local time (LT) and magnetic local time (MLT) instead of time. Local Time is defined as such: the geographic longitude that lies directly on the Earth-Sun line is 12:00 LT. From there as we move westward each one degree of longitude adds four minutes to LT. LT is not a quantity which is provided by our datasets, so our Python 3 code calculates

local time from UTC time and geographical longitude by adding 4 minutes for each longitude to the UTC time of each measurement. This is mathematically formulated as follows:

$$LT = \text{ UT} + 4[\text{ min}] \cdot l \tag{17}$$

where l is geographical longitude $l \in [0, 360]$, and UT is time rounded to nearest minute. MLT need not be calculated in this work, it is instead provided in the dataset compiled by Gieseler et al. (2019). There are a few different ways to calculate MLT, e.g. Laundal and Richmond (2017) recommend the following definition:

$$MLT = \frac{(\phi - \phi_{cd,\mathfrak{s}})}{15} + 12, \tag{18}$$

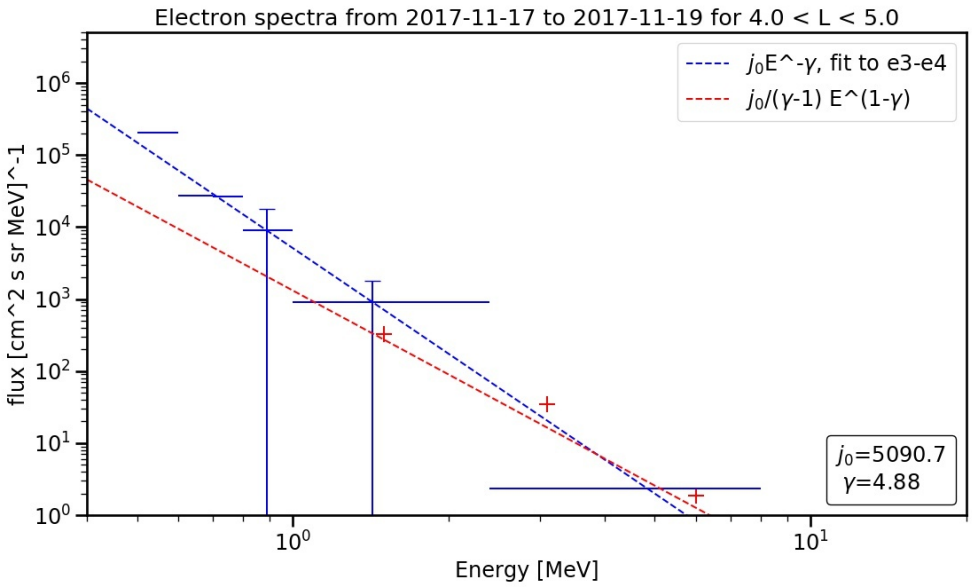

Figure 4. The spectral index effectively gives the slope of the energy spectrum. EPT energy channels and respective intensities are marked with blue horizontal lines. Blue dashed line is the fit through the effective energies on EPT channels e3 to e4. Notice that in our software indexing starts from 0. Red "+" signs signify identically averaged RADMON measurements, and red dashed line is the integrated intensity profile from EPT measurements. Notice that red "+" and the red dashed line have different units than the blue ones.

where ϕ is the magnetic longitude, and $\phi_{cd,\hat{\mathbf{s}}}$ is the centered dipole longitude of the subsolar point. Subsolar point is the point that lies on the surface of the Earth

directly below the Sun. MLT is thus somewhat related to LT, as both are 24 hour-based systems. LT is defined in terms of geographic longitude, while MLT is defined in terms of centered dipole magnetic field longitude. They both still read 12 at the subsolar point.

We divide the x-axis to 24 equally wide bins to represent hours in LT or MLT. We set the y-axis similarly to the multipanel plots, such that it shows a range of L-values from 1 to 10, with bins 0.25 L wide. This again produces a 2-dimensional grid, in which we may plot time-averaged intensity measurements according to the same rules as were described in the Section 2.3.1. Figure 6 presents time-averaged intensity data measured by RADMON over four days, when Aalto-1 observed alternating high

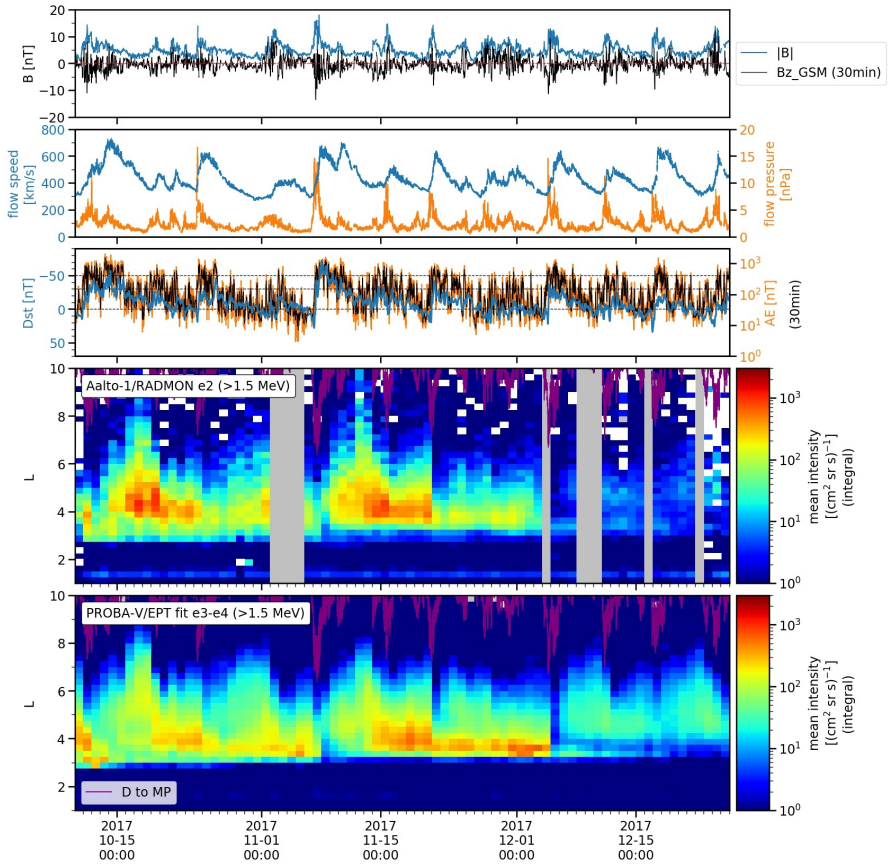

Figure 5. Integrated EPT measurements over the whole dataset. The intensity measurements are plotted with 24-hour resolution.

and low intensities in the outer belt. See Fig. 7 for a timeseries view of this.

4 Results

Using the tools and methods introduced in section 3.3, we will now present the observations and results found from the dataset.

The measured electron intensities of RBSP/REPT are most of the time a thousand times larger than those measured by PROBA-V/EPT. This is due to the different orbits of the spacecraft. Aalto-1 and PROBA-V orbit the Earth in polar SSO at comparatively low altitudes. A polar orbit allows these two spacecraft to go through very large set of different L-values, but the low altitude limits their view of the electron populations on these L-shells. Particles trapped in the geomagnetic

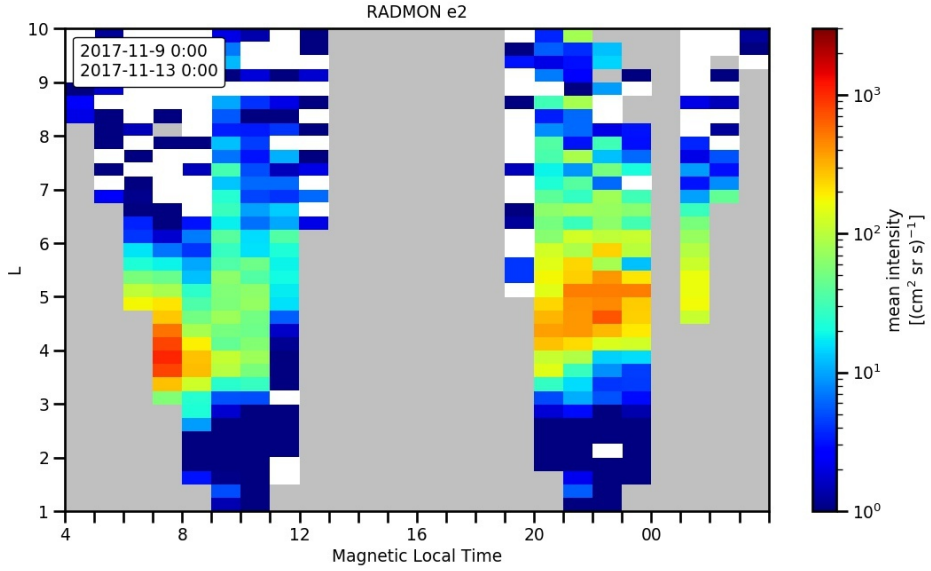

Figure 6. The intensity measurements over a four day period are averaged over into bins of L-parameter and magnetic local time (MLT).

field will mirror back away from the Earth at different points, depending of their pitch angle, and not all electrons will follow magnetic field lines near enough to the Earth for Aalto-1 or PROBA-V to observe them. The RBSP twins on the other hand orbit in a low inclination HEO, meaning they will never see L-values larger than the apogee of their orbit. However, the combination of low inclination and distant apogee allow them to see to the heart of the outer radiation belt, a region where almost all trapped particles will traverse through at least once.

Table IV contains the temporal range of main phase and recovery phase of each storm, as well as the peak negative Dst value achieved at the end of the main phase. We define the moment when $Dst < -15$ nT as the starting point (onset) of the storm and the moment $Dst > -15$ nT as the ending point of a storm.

This kind of definition was also used by Partamies et al. (2013) in their statistical study of substorms. We define the main phase of the storm as the period between the onset and the peak negative Dst value and recovery phase as the period between this peak value and the ending point. If the threshold starting value of $Dst < -15$ nT

Peak Dst [nT]	Onset [MM-DD HH:mm]	Peak	End
-57	10-11 05:30	10-14 05:30	10-16 13:30
-46	10-24 16:30	10-26 14:30	10-27 12:30
-72	11-07 09:30	11-08 01:30	11-11 19:30
-42	11-21 00:30	11-21 06:30	11-21 21:30
-37	12-04 18:30	12-04 20:30	12-06 04:30

Table IV. Magnetic storm events identified from our dataset. Main phase starts when $Dst < -15$ nT and ends when peak $Dst < -30$ nT is satisfied. Recovery phase starts right after the main phase and ends when $Dst > -15$ nT.

is achieved, but Dst does not after that reach the threshold for a small storm ($Dst < -30$ nT) before rising to $Dst > -15$ nT again, then that occurrence is not interpreted as a geomagnetic storm.

Applying these regulations, we identify a total of five geomagnetic storms from our dataset. Two of these storms are moderate and three of them are small. Figure 7 shows a visual representation of finding the onset, peak Dst ,and the end of the storm for the third storm of the dataset. In there one can see that the outer radiation belt is depleted of electrons during the main phase of the storm, which is followed by regrowth of the outer belt during and after the recovery phase. The magnetopause is also pushed in during the main phase.

4.1 Enhancement and Depletion of the Relativistic Electron Belt

During the Oct–Dec period covered by our dataset, we found instances of both enhancement and depletion of the relativistic electron belt associated with geomagnetic storms. By enhancement we mean both an increase in intensity and also the expansion of the outer electron belt. The two strongest storms of this time period both exceed the threshold we use for a moderate storm, which is a Dst index of less

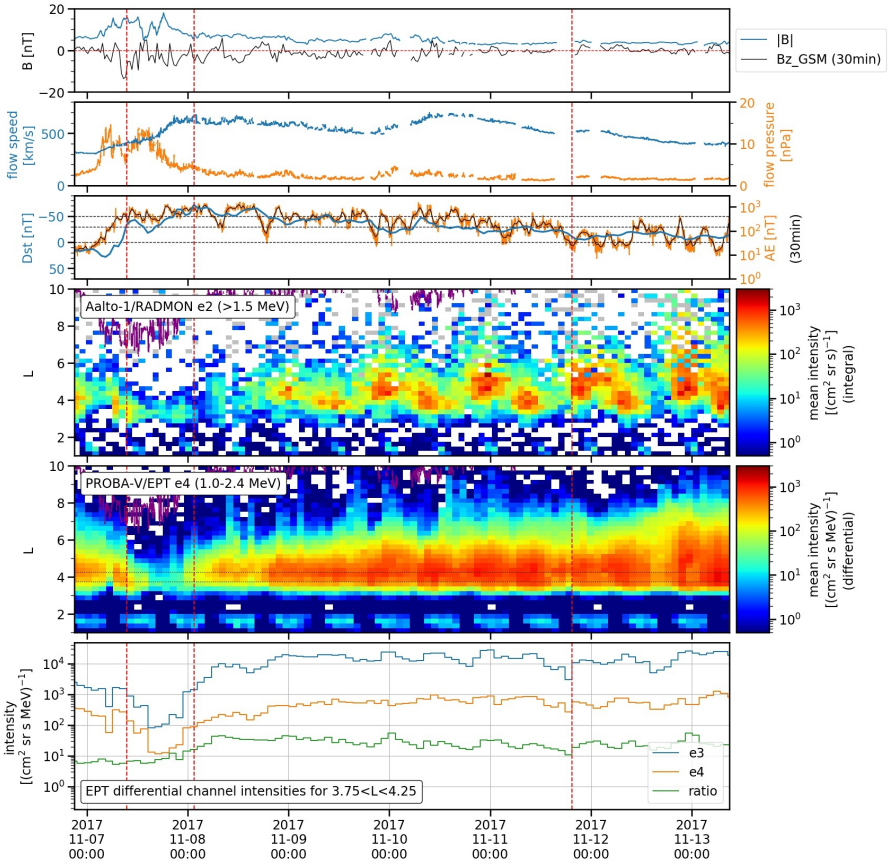

Figure 7. Different phases of the Nov 7 storm in a multipanel timeseries. Main phase of a storm lasts from the moment the Dst index reaches -15 nT to the moment it reaches its peak Dst. Recovery phase starts when the peak Dst is reached and ends when the Dst again rises above -15 nT threshold.

than -50 nT. The first of these two moderate storms occured right at the start of the dataset, lasting roughly from 2017-10-11 to 2017-10-16 with peak $Dst = -57$ nT. The second moderate storm lasted approximately from 2017-11-7 to 2017-11-11 and it had a peak $Dst = -72$ nT. Figure 8 presents the Oct–Nov period and the electron intensity data measured by all four spacecraft. Both of these storms were driven by high-speed solar wind with flow speed peaking at $V > 700$ km/s, which can be seen from the second panel of the figure. The IMF had a comparatively strong turn to the southward direction at the onset of both storms, which is usually a necessity for a storm to commence in the first place. The southward IMF prevailed throughout the storm times, which is indicated by a negative B_z component of the IMF in the

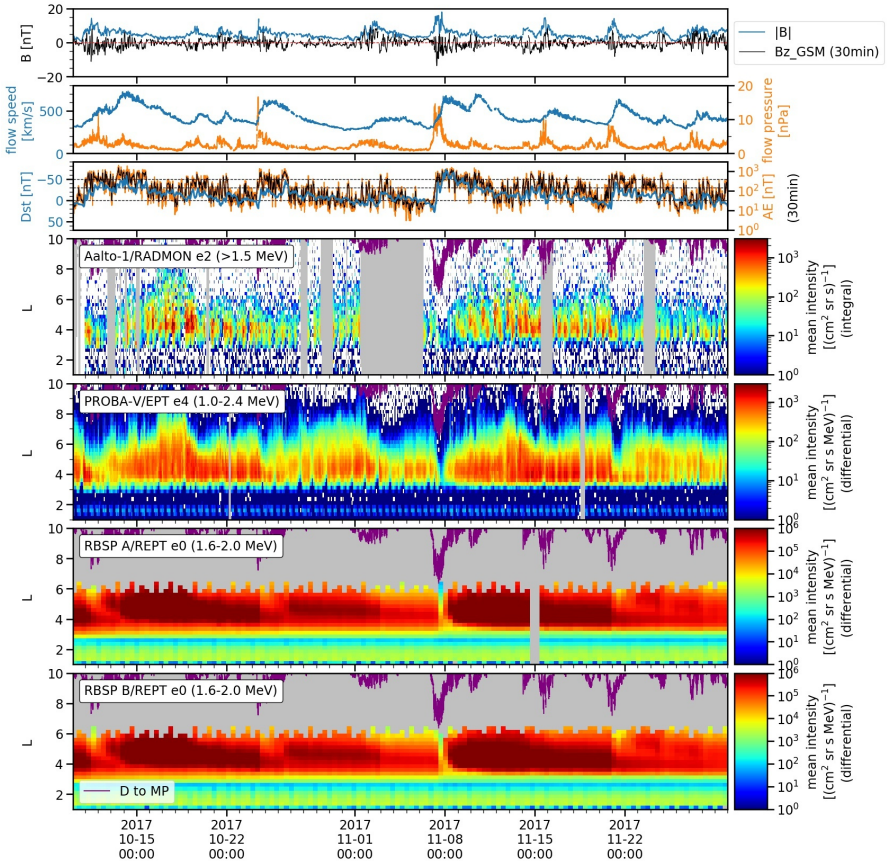

Figure 8. Moderate geomagnetic storm onsets occured on 2017-10-11 and on 2017-11-7. All four spacecraft of the three missions observe the enhancement associated with the recovery phases of these storms and the sudden and short-lived depletion of the outer electron belt during the main phases of them. Temporal resolution in intensity plots has been set to the orbital period of the respective satellite.

first panel. All of the three missions employed in this thesis observed increased electron intensities in the outer radiation belt during the recovery phases of these storms. On top of an increase in measured intensities, Aalto-1 and PROBA-V also observe expansion of the outer belt to $L > 8$. Preceding both storm onsets, the dayside of the magnetopause was pushed closer than 8 Earth radii distance, which is plotted as purple on all four intensity panels. The storms commence with a decrease in the *Dst* index, which in the case of the Oct 11 storm is slow in comparison to the rest of the storms. Especially in the case of the Nov 7 storm the depletion of the outer belt is sharp, visible on practically all L-values, and fits particularly well

within the boundaries of the main phase. It is a good example of a strong dropout event, which affects the entire outer electron belt. A dropout event means a fast depletion of the outer electron belt on a range of L-values.

The shrinking of the outer electron belt prior to the two moderate storms were not the only such occurrences in the dataset. There was a dropout event on 2017-11-21 and one more gradual depletion on 2017-10-24. Both of these events were observed by all four spacecraft, though the RBSP twins only saw them partially, due to their limited view of L-shells. In these events the measured intensities decrease at $L > 5$, but not elsewhere. Figure 9 shows intensity measurements during December for all spacecraft. The strong depletion of Dec 4 was observed very clearly by all four spacecraft and it is as a dropout event similar to the one on Nov 7. There is an unfortunate gap in RADMON data coinciding with this event, but the rest of the spacecraft all observe decreasing intensity at all L-values. All in all, we observe a clear and sudden depletion of the outer belt associated with the main phase of a geomagnetic storm in three of the five storms in our dataset. Chronologically the first two storms (Oct 11 and Oct 24) also display some shrinking of the outer electron belt, but the effect is more gradual and weak than with the strong dropout events occurring in a matter of hours, during the main phases of the last three storms.

Figure 10 shows the temporal evolution of the shape of the outer belt during and after the Oct 11 and Oct 24 storms, observed by PROBA-V/EPT. It is the case with both of these storms, that the outer belt shrinks after the storm onset and then expands again after the main phase is over. Both storms are also characterized by very long and gradual main phases. During the Oct 11 storm, the outer belt expands to higher L-values than the pre-storm outer belt, while the peak intensity does not reach as high as before the storm. It is already the case during the shrinking of the belt that as the peak of intensity decreases, the extent of the belt simultaneously grows to larger L-values. At $L = 4$ the intensity is decreasing as time passes, while

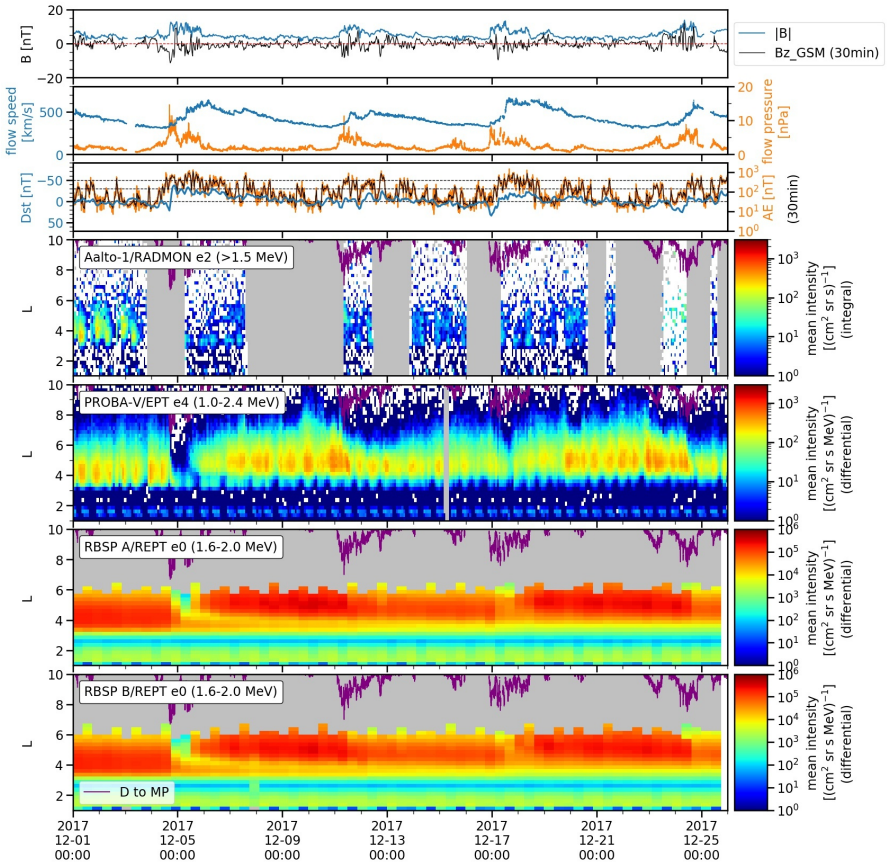

Figure 9. A small geomagnetic storm onset occurred on 2017-12-4, causing a noticeable depletion in the outer electron belt during its main phase. In December, the high intensity part of the outer electron belt is 0.5 L higher than in the preceding months.

at $L > 5.5$ the opposite is happening.

The Oct 24 storm is different. The intensity is seen to decrease at all L-values during the main phase, even around $L = 3$. The outer belt is at its smallest at 20:12 on Oct 24, after which regrowth of the belt begins. However, even after two days have passed after the onset, the outer belt still has not grown back to its pre-storm size. At 22:42 on Oct 26 the measured intensity is lower at all L-values than it is before the storm onset.

Figure 11 presents the evolution of the shape of the outer electron belt during the rest of the storms. The Nov 7 storm has a strong dropout event during its main phase and this is reflected in Fig. 11 as well. The intensity at $L = 4$ decreases

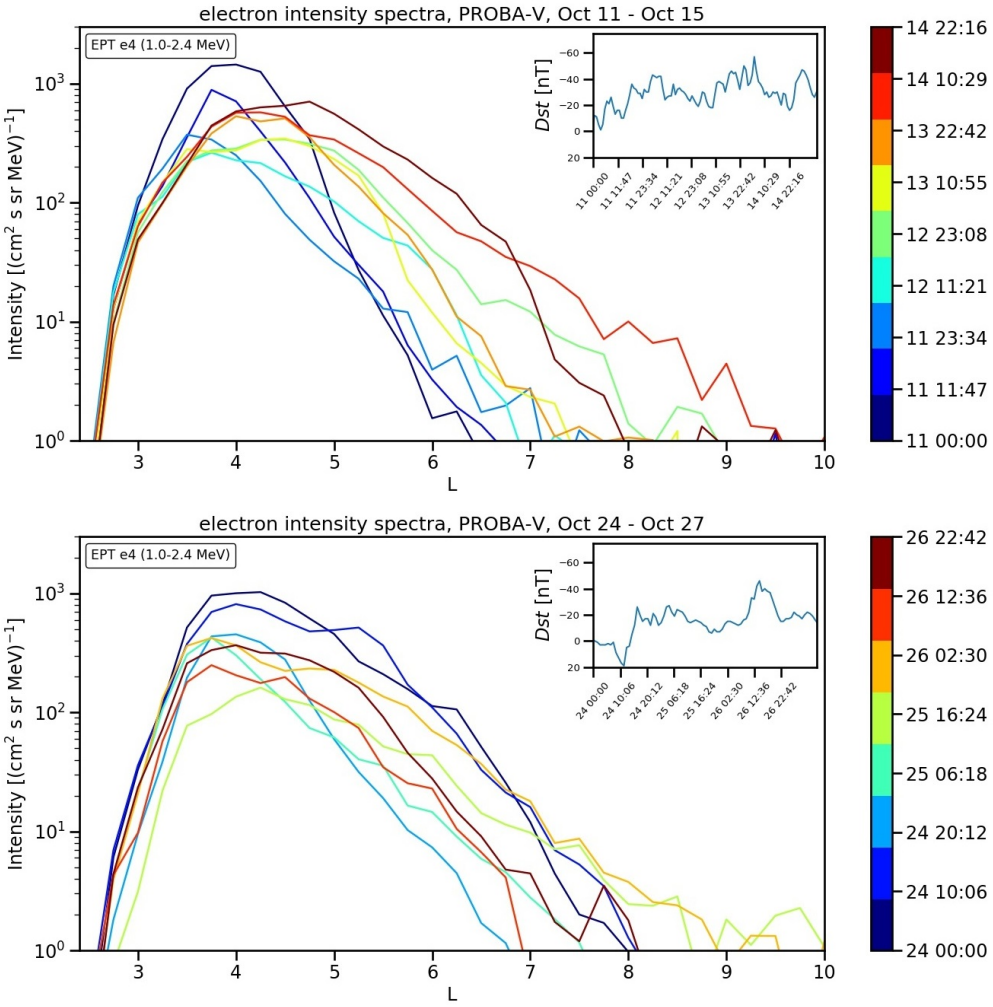

Figure 10. The electron intensity as a function of L at different times during the two October storms. The intensity plotted for each time is time-averaged over one orbit (101 minutes). The top right corner shows the *Dst* index at corresponding times. The color coding shows the day of the month followed by UTC time.

by an order of magnitude between 06:44 – 20:12 and beyond $L = 6$ to less than 1 $\mathrm{cm}^{-2}\mathrm{sr}^{-1}\mathrm{s}^{-1}\mathrm{MeV}^{-1}$. Similarly to the Oct 24 storm, the intensity decreases also around $L = 3$ during the main phase. At 05:52 on Nov 9, the intensity has increased higher than the pre-storm belt at all L-values, except for $L = 7$. We know from the multipanel plots that the outer belt grows larger than before the storm after the recovery phase of this storm is over, but this is not yet reflected in Fig. 11.

In the case of the Nov 21 storm, the outer belt is practically depleted of $E >$ 1 MeV electrons at $L > 6$ by 08:12 on Nov 21. The decrease in intensity is more

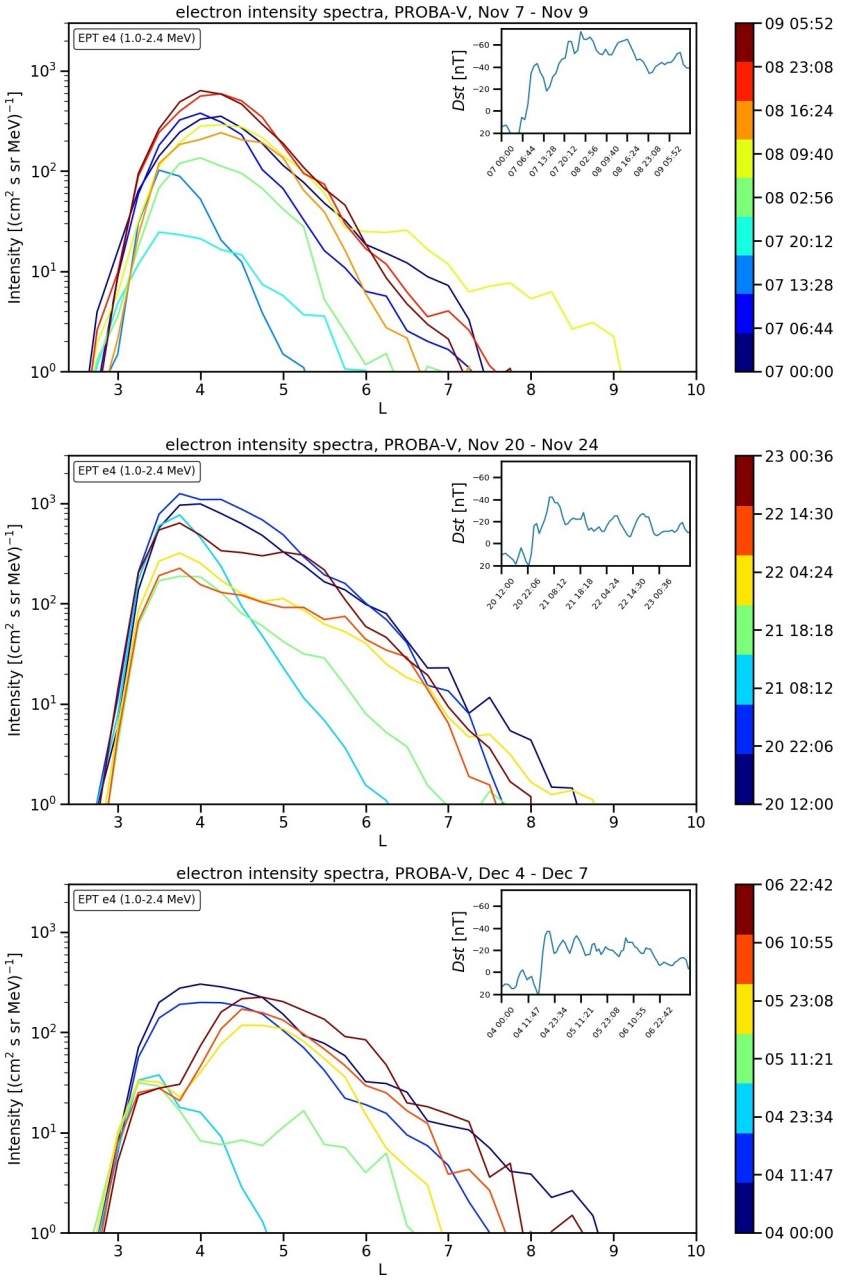

Figure 11. The electron intensity as a function of L at different times during the Nov 7, Nov 21, and Dec 4 storms. The intensity plotted for each time is time-averaged over one orbit (101 minutes). The top right corner shows the Dst index at corresponding times. The color coding shows the day of the month followed by UTC time.

gradual at around $L = 4$, but by 18:18 on Nov 21, the intensity has decreased by an order of magnitude also there. The outer belt starts to expand at $L > 5$ only after the recovery phase is already over. At 00:36 on Nov 23, the measured intensities at

$L > 5$ have nearly risen to pre-storm conditions. At $L = 4$, however, the intensity remains lower than the pre-storm intensity.

The Dec 4 storm completely changes the shape of the outer belt, unlike any other storm observed in the dataset. At $L = 3$, the intensity remains roughly constant during the storm. However, the intensity decreases rapidly everywhere else during the main phase and at 23:34 on Dec 4, the intensity even at $L = 5$ is less than 1 $\mathrm{cm^{-2}sr^{-1}s^{-1}MeV^{-1}}$. The strongest increase in the intensity is seen around $L = 5$ after the main phase, whereas during all other storms of the dataset the peak intensity has always been around $L = 4$. At 22:42 on Dec 6, the outer belt has grown back to its pre-storm extent. However, even two days after the onset there still remains a deficit in the intensities at $3 < L < 4$.

To quantify the extent of the shrinking and expansion of the outer belt, we set a threshold value of 50 electrons/($\mathrm{cm^2}$ s sr MeV) as a limit, to find the outer edge of the outer belt. Every orbit the L-value at which the intensity first drops under this threshold value in the outer belt is considered to be the outer edge of the outer belt. This is shown in Fig. 12, plotted over EPT 1.0–2.4 MeV measurements. In their study of electron flux dropout events, Pierrard et al. (2020) set a threshold of 100 electrons/($\mathrm{cm^2}$ s sr MeV) for 0.5–0.6 MeV electrons. We find that by our definition, the outer belt peaks momentarily to at most $L = 9.6$ and drops to $L < 3$ during two dropout events. The peak is achieved on Oct 16 20:58, which is over seven hours after the recovery phase of the Oct 11 storm has ended. The two complete dropouts, when the outer edge reaches $L < 3$, occured on Nov 7 16:29–21:32 and on Dec 5 09:24–11:05.

Despite the sharp drops that happen in conjunction in both the belt edge and the dayside magnetopause plotted in Fig. 12, no definite linear correlation was found between them. Figure 13 shows four scatter plots of the outer belt edge with some of the other data used in the study. We calculated the Pearson correlation coefficient

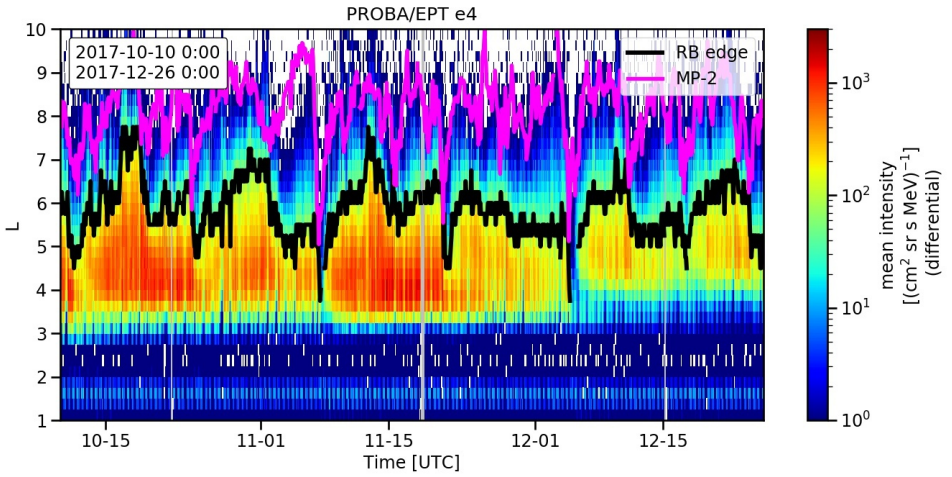

Figure 12. EPT electrons in the 1.0–2.4 MeV channel. Black line represents the 50 electrons/(cm^2 s sr MeV) threshold, and magenta line is the distance to the dayside magnetopause shifted down by 2 L.

for these pairs and found that the absolute value of the Pearson's r was less than 0.5 for all of the pairs. The Pearson's r is a statistical measure of the linear correlation between two sets of data, which yields $r = 1$ for two perfectly correlated sets and $r = 0$ for two sets with no linear correlation at all. The best correlation with the outer belt edge was with the strength of the IMF, which was $r = -0.457$.

4.2 Estimating the Electron Energy Spectrum

There is an apparent discrepancy between the observations of Aalto-1 and the other spacecraft in December. The start of a dropout event is observed by PROBA-V and the RBSP twins on Dec 4, during the main phase of the Dec 4 geomagnetic storm. This is shown in Fig. 9.

Aalto-1 observes this dropout event only partially. PROBA-V and the RBSP twins then observe regrowth of the outer belt, starting on Dec 5. Aalto-1, however, does not observe this regrowth of the outer belt. Instead, RADMON measurements suggest that the integral intensity in the entire outer belt does not grow back to the level of the preceding months. A possible explanation to this discrepancy is that the

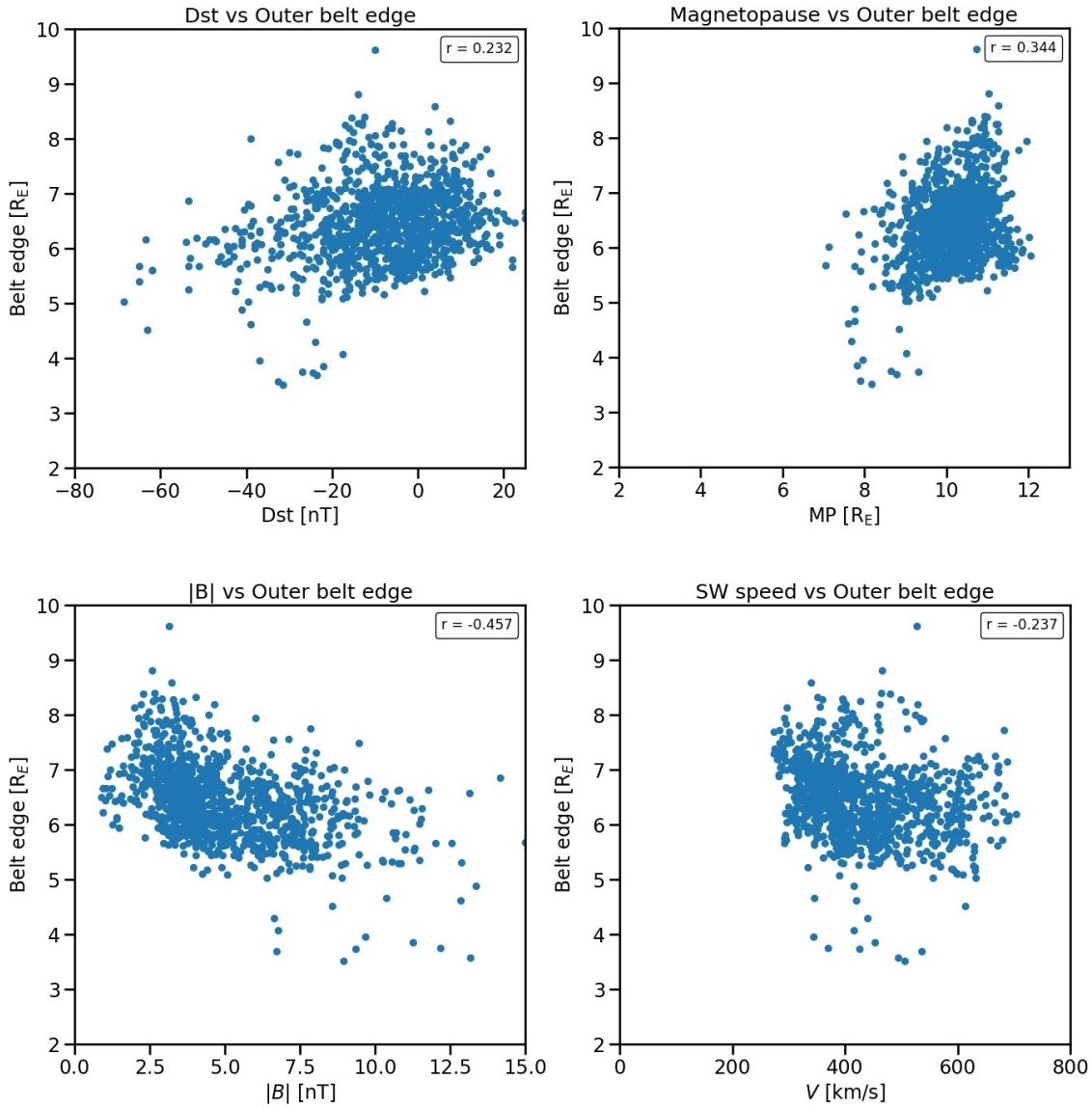

Figure 13. The outer belt edge, identified by the threshold of 50 electrons/(cm^2 s sr MeV), plotted with the *Dst*, dayside magnetopause distance, IMF strength, and the speed of the solar wind. The Pearson correlation coefficient for the respective pairs is shown in the top right corner of each plot.

energy spectrum of the electron population may have turned softer after the Dec 4 storm. By a soft spectrum, we mean an energy spectrum that has steep slope, and thus, less high-energy electrons. A soft spectrum is described by high spectral index, while a hard spectrum would be described by a low spectral index. Should the energy spectrum turn softer than it has previously been, then an instrument

measuring integral intensity would observe this as a major change. However, an instrument measuring differential intensity would not necessarily observe any major change in intensity, depending on the energy channel one is looking at. This is because a softer energy spectrum does not necessarily mean that there are any less lower energy electrons than before.

To better compare the measurements of RADMON and EPT, we calculate the expected integral intensity profile based on the EPT measurements. The integration method is described in section 3.3.2. Figure 14 shows a comparison between RADMON and integrated EPT measurements in December, when the measurements disagreed the most. During December, the calculated integral intensity profile based on measurements from EPT's electron channels 4 and 5, agrees better with those of RADMON's. The calculated integral intensity is still in some regions an order of magnitude higher than the corresponding RADMON measurements. This can at least partly be explained by the fact that Aalto-1 orbits the Earth at an altitude, which is on average over 300 km lower than PROBA-V's altitude. Only a portion of all the electrons on a given L-shell have small enough pitch angle to follow a magnetic field line to a 500 km altitude, before bouncing back due to magnetic mirroring. Thus, we would assume that two identical particle detectors at different altitudes measure different integral intensity anyway. The integrated EPT measurements seem to agree with those of RADMON's in October and November as well, as they should if these two instruments measure the same particle population.

The spectral index is calculated from EPT measurements as part of the integration process. This also allows for plotting γ to the multipanel timeseries against the L-values, as was done with the actual intensity measurements. Figure 15 shows the spectral index calculated from EPT measurements in the bottom panel. Notice that the colorscale for γ is inverted to make hard spectra stand out better with red color. A hard spectrum means that the spectral index is low, which means that the

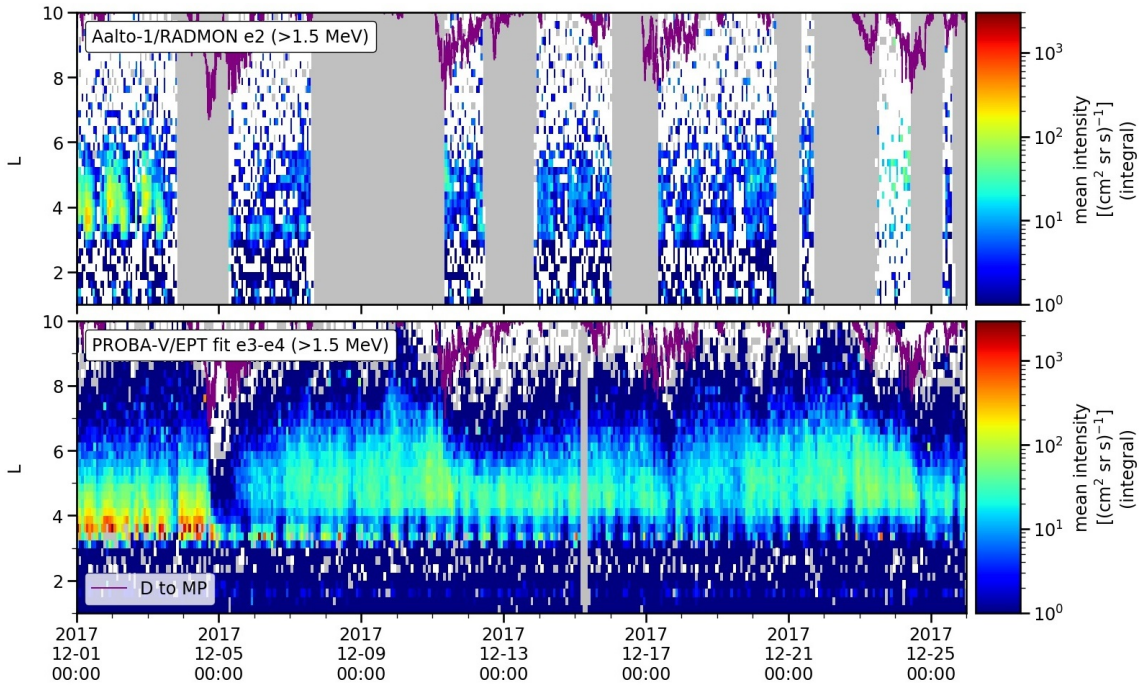

Figure 14. A comparison between Aalto-1/RADMON integral intensity measurements and PROBA-V/EPT calculated integral measurements during December 2017.

slope of the energy spectrum is less steep.

It seems to be a dominant trend all throughout the dataset that the energy spectrum is particularly hard in $3 > L > 4$. We call this region the inner edge of the outer electron belt. In there, the spectral index is mostly $1 < \gamma < 3$. The only exception to this occurs during the Nov 7 moderate geomagnetic storm, which seems to steepen the spectrum of the electron population for over a week. The hard part of the spectrum starts to soften from the higher L-values first and gradually from lower ones as well. The hard spectrum returns after Nov 16, starting from higher L-values towards lower ones. The dropout event in the outer electron belt on Dec 5 also has some effect to this hard spectrum population, as it coincides with the hard part of the spectrum shrinking abruptly to only cover roughly the L-values of $3 < L < 3.5$. Outside this hard spectrum region, the ambient spectral index is mainly $4 < \gamma < 7$. The values below $L = 3$ we do not consider here because that region does not belong in the outer radiation belts.

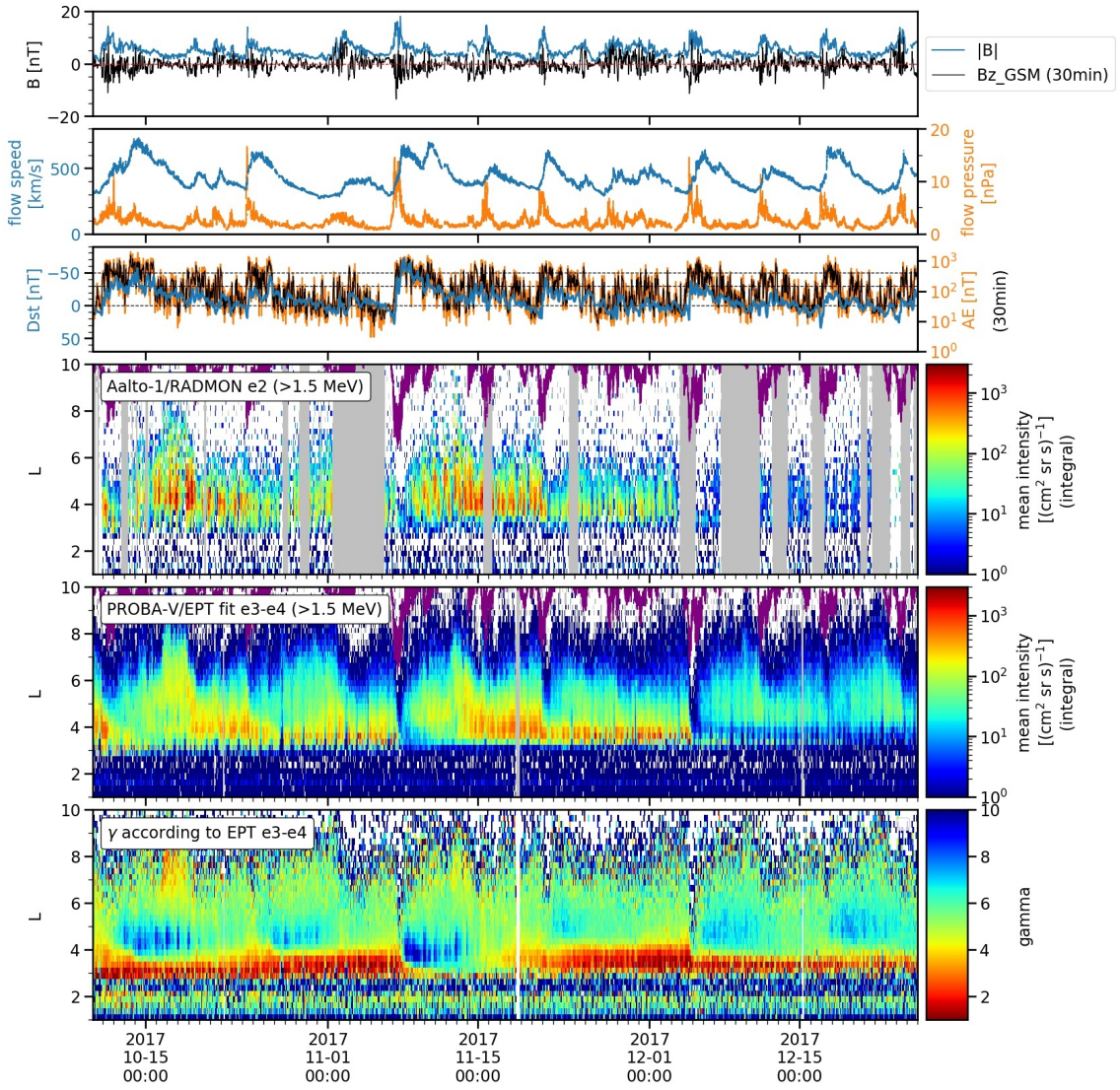

Figure 15. The spectral index is plotted on the grid in the bottom panel according to PROBA-V / EPT measurements. We find an alternating pattern in the energy spectrum, which emerges periodically roughly every two weeks. The pattern is particularly strong during the two moderate geomagnetic storms starting at Oct 11 and Nov 7.

Figure 16 is a plot of L-value averaged intensity data, averaged over the hard spectrum region, from the channels we use to calculate the spectral index. The ratio of the consecutive differential channel intensities there is most of the time less than 10. When the hard spectrum part is softened during the Nov 7 storm, the ratio of the channels quickly increases to over 30. This is caused by a large increase in the lower electron channel that measures energies 0.8–1.0 MeV. The intensity in the

higher channel that measures energies 1.0–2.4 increases much more gradually, which leads to the softening of the energy spectrum.

There is also a recurrent alternating pattern in the spectral index that appears roughly every two weeks and is especially strong in conjunction with the moderate geomagnetic storms. This pattern, which is visible in Fig. 15 as blue vertical stripes, has to do with the spectral index alternating between lower and higher values. The blue vertical stripes are embedded in a cyan halo, which means that the ambient spectral index during the alternating pattern is $6 < \gamma < 7$, whereas outside the pattern it is $4 < \gamma < 5$. The alternation is most noticeable during the two moderate storms, the first one beginning on Oct 11 and the second one on Nov 7. The pattern is visible also on four other instances. They have beginnings on Oct 25, Nov 22, Dec 5, and Dec 17. Figure 17 is a zoomed in window to the storm time spectral index during the Nov 7 storm, which better shows the alternating high spectral index pattern.

We estimate the temporal length of the alternating pattern by using the ambient spectral index. When the ambient spectral index between $4 < L < 5$ is $\gamma > 6$, then the pattern is still there. The first one, starting on Oct 11 lasted the longest, which was approximately seven days. The shortest span was with the pattern of the Nov 21 storm, which was three days. The other patterns all had a duration of roughly six days. The range of L-values these patterns cover was also rather constant, with the main part of the very soft spectrum regions fitting between $4 < L < 5$. The only exception to this was the moderate storm starting on Nov 7, for which the main part of the pattern expanded downward to $L = 3.5$. The values of γ during these events alternated between $6 < \gamma > 10$, whereas the ambient spectral index in the outer electron belt is $4 < \gamma < 5$.

In December, the alternating patterns are not as strong as they are during the two storms of October and the moderate one on Nov 7. The ambient spectral index

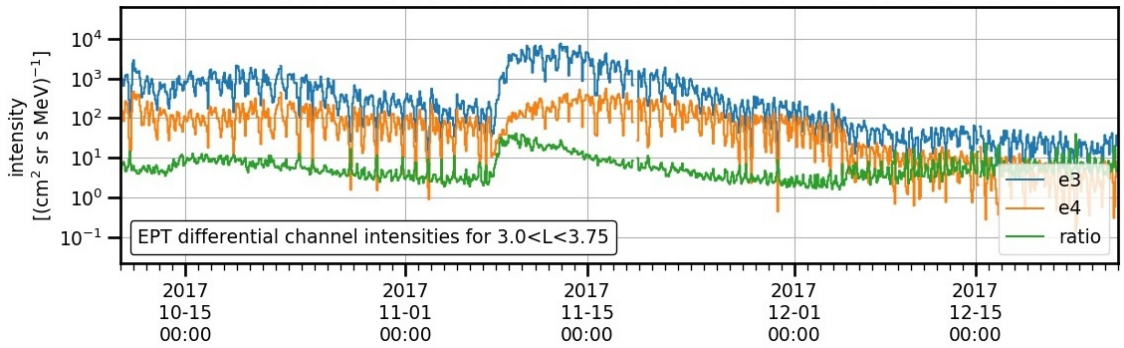

Figure 16. The intensities of the two differential channels of EPT that we have used for calculating the spectral index, averaged over the L-parameter from 3.0 to 3.75. This range covers the region of very hard spectrum seen in Fig. 15 as red. During the Nov 7 storm, there is a strong two orders of magnitude growth in the lower energy channel. Both channels also measure a short decrease just before the intensity increases.

there is $\gamma \approx 6$. The hard spectrum region in Fig 15 is also thinner than in the preceding months. Overall, the energy spectrum between 0.8–2.4 MeV is softer during the whole December in comparison to October and November.

4.3 RADMON High Intensity Pattern

There is a pattern of recurrent high intensity seen by RADMON that manifests itself in November during the expansion of the outer electron belt. The pattern is clearly visible in Fig. 17, which is the third storm of the dataset. The figure also shows quite well how this recurrent pattern seen by RADMON overlaps with the alternating spectral index calculated from EPT measurements. Characteristic to this high intensity pattern is that high intensities seem come in pairs with the first burst hitting higher L-values than the second one. When averaging the intensities over the time period of interest, as we have done in Fig. 6, we see that the high intensities concentrate at magnetic local times MLT = 8 and MLT = 22. The concentration of high intensity on the night side appears at a higher L-value and more spread out.

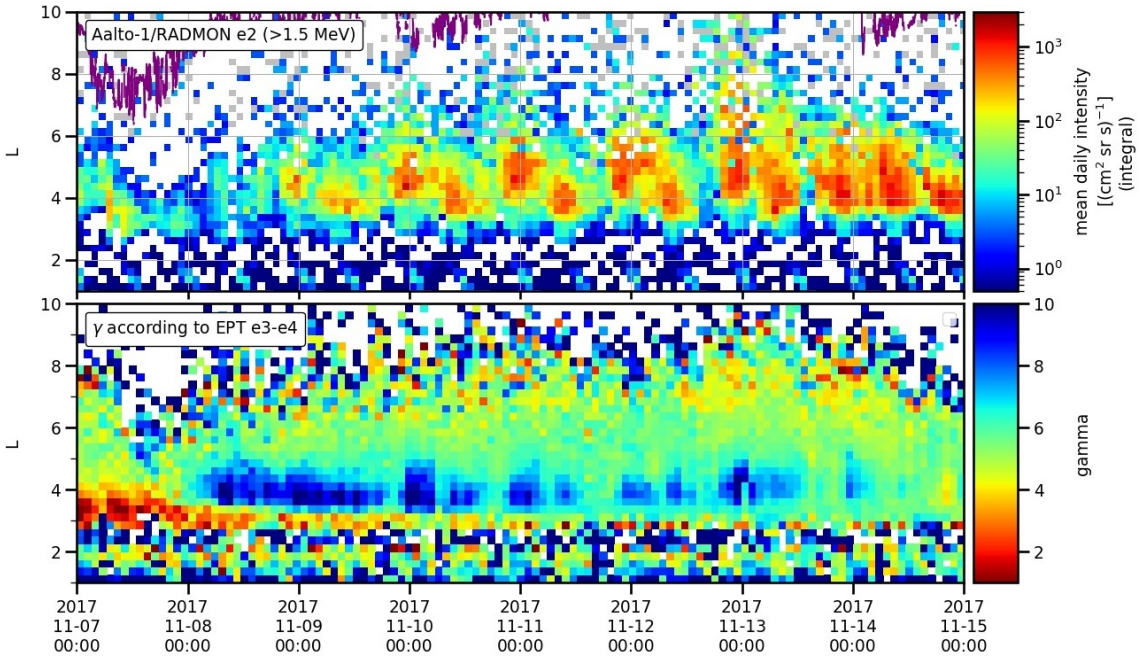

Figure 17. A zoom-in to the time frame surrounding the moderate geomagnetic storm, which started on Nov 7. The panels show RADMON channel e2 measurements and the spectral index calculated according to EPT channels e3 and e4. The region where the energy spectrum varies is mostly constrained to 3.5<L<5 and it lasts approximately 6 days.

5 Discussion

In this chapter we discuss the potential sources of errors and biases of this study. We also give our interpretation of the objective observations presented in chapter 4.

Solar wind speed and pressure, the IMF, *Dst* index, and *AE* index are all included in the OMNI data. OMNI datasets are compiled from multi-spacecraft observations at L_1 (Lagrange point 1), which are then time-shifted to the nose of the Earth's bow shock. The time-shift in itself is an estimate, and thus brings some uncertainty. Flow pressure of the solar wind is calculated from flow speed and proton density of plasma, and proton density is known to usually have poor statistics compared to, e.g. IMF measurements. This carries out to flow pressure having small data gaps all throughout the dataset. Since we calculate the nose of the

magnetopause according to Eq. (3) (Shue, 1997), which takes pressure of the solar wind as an input, that too will have the same data gaps. The magnetic indices, Dst and AE, are provided in the OMNI dataset but are initially provided by the World Data Center for Geomagnetism, Kyoto. Dst is derived from magnetometric measurements done in four different observatories independent of each other. The Dst index is only available with an hourly resolution, but that will suffice since we employ it as an indicator of different storm phases.

The electron intensity data of RADMON has somewhat poor statistic in comparison to those of EPT's and REPT's. There are also unfortunate data gaps in RADMON data that prohibit us from seeing the start of November and the majority of December from the point of view of Aalto-1. The intensity data in the multipanel plots is put into discrete bins and the value of each bin is calculated as the arithmetic mean of the measurements in that bin. The highest temporal resolution in multipanel plots for any singular bin is the orbital period of the corresponding satellite because it ensures that all the possible L-values get covered in each vertical time bin. Since any vertical bin in the multipanel plots will contain measurements from an entire orbit, we expect the possible erroneous measurements to have little impact on the average value that is calculated for each bin. There are instances of horizontal bins that contain very few measurements, such as those at high L-values, but their effect on the analysis conducted primarily at $3 < L < 7$ is minor.

The spectral index is calculated by an iterative method that stops once the difference between two consecutive values is less than 0.1. Therefore, that is the accuracy we have for γ. The plots do not represent the actual energy spectrum at all energies because they are calculated with measurements from only two channels. Note that we have also assumed that the electron energy spectrum is a power law, which is not necessarily true at all times. Especially during the depletion and enhancement of the outer belt, we expect the spectrum to not be a strict power law since different

processes accelerate electrons of varying energy at different rates. As an example, Fig. 16 shows how a sudden influx of lower energy electrons may completely change the spectral shape in a short amount of time.

Another thing about the calculated spectral index is that it primarily defines the integrated intensity function we use to compare the observations of PROBA-V and Aalto-1. The low resolution picture in Fig. 5 shows that the integrated EPT measurements agree quite well with the corresponding RADMON measurements regarding the overall shape of the outer electron belt. Also the specific intensity values agree most of the time, though there still are few instances of a discrepancy. During the recovery phase of the Oct 11 storm when the outer electron belt is extended to $L > 8$, RADMON measures high integral intensity in the region $4 < L < 5$ until Oct 19. Our expected integral intensity from EPT does not reproduce this high intensity region during the expansion. The EPT calculated integral intensity does, however, expect high intensity at the inner edge of the outer electron belt ($3 < L < 4$) at the start of December, although RADMON sees no such thing.

The geomagnetic storms in the dataset are for the most part not typical textbook examples of magnetic storms. In terms of the *Dst* index, a typical textbook storm has small positive bump preceding the onset. The onset is rapid and recovery follows steadily, spanning for the majority of the storm time, after achieving peak *Dst* (Koskinen, 2011). Of all the storms in our dataset, the Nov 7 moderate storm resembles a textbook storm the most. The positive bump, very quick negative turn in *Dst*, and a comparatively long recovery phase all characterize this storm. All instruments employed in this study also agreed that the radiation belts underwent a depletion during the main phase of that storm. This storm also enhanced the outer electron belt during its recovery phase and after it.

Out of the five storms in our dataset, we found that the outer electron belt was enhanced (that is, expanded and intensified) in the aftermath of three storms, two of

which were moderate storms. The enhancement starts already in the recovery phase of a storm and continues even after that. The outer electron belt was expanded to at most $L = 9.6$ after the moderate storm that commenced on Oct 11. In comparison to Reeves et al. (2003), who found enhancement for 53 % of moderate or intense storms, we are in good agreement if we also include the small storms of our dataset. Also Turner et al. (2015) found that for the core population of electrons ($E > 1$ MeV) in the region $L > 4$, the frequency of enhancement and depletion events is quite evenly distributed, which is the case for this study as well. Since this study consists of only CIR-driven storms, we would also agree with the later study by Turner et al. (2019) that suggests that SIRs are highly effective at enhancing multi-MeV electrons at $L >\sim 4.5$. Note that Turner et al. (2019) constrained their dataset to storms of SYM-H ≤ -50 nT, which is a different metric than Dst index. However, Wanliss (2007) found that SYM-H should not deviate from Dst during small or moderate storms much more than 10 nT, so the conclusions should apply to studies using Dst as well. Bingham et al. (2018) agrees with the aforementioned study, their study suggesting the greatest flux increase for CIR-driven storms between $4.5 < L^* < 5.0$. Even though L^* is an intrinsic property of a particle and not a spatial coordinate like L, they are still very comparable especially near the equatorial plane.

Because the magnetopause was pushed in near the main phase of all the storms, as one can see from Figs. 8 and 9, magnetopause shadowing was probably a major contributor of depleting electrons at the higher L-values. It has been suggested that magnetopause losses coupled with outward radial diffusion are mechanisms that efficiently deplete the outer belt of energetic electrons even at low L-values. Radial outward diffusion acts during the main phase of a storm because the enhanced ring current causes electrons to move radially outward to conserve the third adiabatic invariant (Millan and Thorne, 2007).

During the Oct 11 storm electron intensity at $L \approx 3$ does not noticeably change,

as is shown in Fig. 10 (top). This is likely a sign of weakened electron precipitation at the inner edge of the outer belt. To know exactly what halts electron precipitation at that time one would need knowledge of the local magnetic field, which is something to consider in the future. The fact that electron intensity is observed to rise at $L > 5.5$, while at $L \approx 4$ the opposite is happening, suggests that outward radial diffusion is likely expanding the outer belt.

The decrease of intensity at $L < 3$ during the Oct 24 storm is a sign of precipitation. The outer belt is seen in Fig. 10 (bottom) to expand to $L > 8$ during the main phase after the initial decrease, which is likely explained by outward diffusion. The electrons are then again depleted from $L > 8$ by 12:36 on Oct 26 probably due to magnetopause shadowing. The second Dst peak seen at this time is also an indication of outward radial diffusion preceding it. The increase of intensity around $L = 4$ after 16:24 on Oct 25 could be a local acceleration process since intensity also increases at $L = 3$ at the same time. However, without knowledge of the phase space density it is difficult to exactly state whether it was local acceleration or inward radial diffusion that increased the intensity (Reeves et al., 2013).

The Nov 7 storm seen in Fig. 11 (top) effectively depletes the outer electron belt during the main phase. The magnetopause is at that time particularly close to the Earth, which definitely indicates strong magnetopause shadowing. The intensity at $L \approx 4$ increases to higher than the pre-storm intensity, indicating almost certainly local acceleration of the electrons. The belt is extended to $L = 9$ at 9:40 on Nov 8 but contracted to pre-storm extent after that, indicating inward radial diffusion to be a contributor of increasing intensity at $L < 7$.

The intensity around $L = 3$ during the Nov 21 storm is again an indication of weakened precipitation at the inner edge of the outer belt. This is shown in Fig. 11 (middle). The outer belt is strongly depleted of electrons at $L > 6$ by 8:12 on Nov 21 indicating magnetopause shadowing, but not necessarily strong outward

radial diffusion because the intensity around $L = 4$ has not changed much then. After 18:18 on Nov 21 the intensity is seen to increase first at $L > 5$ before finally increasing at $L = 4$. This suggests that outward radial diffusion only started after the main phase of the storm passed.

The main phase of the Dec 4 storm is extremely short in comparison to the other storms that have been discussed. The decrease in intensity in Fig. 11 (bottom) is seen to start at high L-values first, again likely due to magnetopause shadowing. Precipitation at $L = 3$ is again weakened during the storm. After the main phase, at 23:34 on Dec 4, the outer belt is effectively depleted of electrons. Since the intensity is then seen to increase at $L > 4.5$ but not lower than that, outward radial diffusion is likely expanding the outer belt. Effectiveness of inward radial diffusion seems to be greatly weakened at lower L-values, which is indicated by the fact that the intensity at $L = 4$ does not increase back to pre-storm level for an extended period of time. This results in the peak intensity of the outer belt electrons to shift further away from the Earth.

The outer edge of the outer belt, which is plotted in Fig. 12, has sharp drops in conjunction with the distance to the nose of the magnetopause. This is especially the case during the two complete dropout events on Nov 7 and Dec 5. However, the Pearson correlation coefficient was not found to be particularly high between the outer belt edge and other variables. Some of the highest correlations are presented in Fig. 13. The highest linear correlation was found between the outer belt edge and the strength of the IMF, which was $r = -0.457$. The moderately negative correlation coefficient indicates that we are more likely to observe shrinking of the outer electron belt during times of stronger IMF.

6 Conclusions and Outlook

We have examined a part of the relativistic electron population in the outer radiation belt during geomagnetic storms that were driven by fast solar wind flows in autumn of 2017. We found that during all five storms the outer electron belt was shrunken in the main phase of the storm. The sudden shrinking of the outer belt is known as a dropout event. During two of these dropout events the threshold-specific outer edge of the outer belt reached $L < 3$, indicating an effective depletion of the $E > 1$ MeV electrons. No conclusive linear correlation was found between the threshold-specific outer edge of the outer belt and other variables.

We found that the outer electron belt was enhanced in the aftermath of two moderate and one small geomagnetic storms. Enhancement in the outer belt means both increase in the intensity of the electron flux and the expansion of the belt to higher L-values. We also found that the energy spectrum of the outer belt electrons was softened for an extended time period after a dropout event associated with the main phase of a geomagnetic storm.

Figures 10 and 11 show the 1.0–2.4 MeV electron intensity as a function of the L-parameter during each individual storm, according to the measurements of PROBA-V/EPT. The peak intensity is close to $L = 4$ during all but one of the storms, regardless of storm phase. During the small storm of Dec 4, after an intense dropout event, the peak intensity of the outer electron belt was transferred to around $L = 5$ for an extended period of time.

Furthermore, we have observed that at least the $0.8-2.4$ MeV part of the electron energy spectrum alternates in the $3.5 < L < 5$ region, achieving values of $\gamma > 10$, during the recovery phases of geomagnetic storms driven by fast solar wind. The effect is stronger for moderate storms than for small storms, but the temporal span does not seem to be strongly related to the strength of the storm.

For the future, the pitch angle distribution of the electrons would be helpful data

to process since it could help us better consider electron precipitation as a process that depletes the outer belt during storm main phases. The REPT instrument aboard RBSP, for example, is able to provide accurate pitch angle measurements (Baker et al., 2013). One of the main objectives of the RBSP mission was also to investigate different acceleration mechanisms in the outer electron belt (Mauk et al., 2013).

Another way to extend this study would be to look into the remaining electron channels that we did not really employ during this work. In this thesis, practically the only instrument we used multiple channels from was the EPT of PROBA-V. Especially the electron population's spectral shape is based on only two energy channels, from the point of view of a single satellite. The REPT of Van Allen Probes would also allow for studying the spectral shape via a fit to different energy channels. The Van Allen Probes could be employed more in other aspects as well because farther from the Earth they see a larger portion of the trapped electron population than PROBA-V and Aalto-1 on LEO. More accurate map of the spectrum could be modeled by using more energy channels and possibly assuming a broken power law with a separate high-energy tail.

Acknowledgements

Part of this thesis work was performed while working as a research assistant at the Space Research Laboratory, University of Turku, which is gratefully acknowledged. The author is thankful for the advice received from several colleagues at Space Research Laboratory and for the steady supervision of Dr. Gieseler.

Processing and analysis of the REPT data was supported by Energetic Particle, Composition, and Thermal Plasma (RBSP-ECT) investigation funded under NASA's Prime contract no. NAS5-01072. All RBSP-ECT data are publicly available at the Web site http://www.RBSP-ect.lanl.gov/

The *Dst* and *AE* indices used in this publication were provided by the WDC for Geomagnetism, Kyoto (http://wdc.kugi.kyoto-u.ac.jp/wdc/Sec3.html). OMNI data is publicly available via, e.g. cdaweb.gsfc.nasa.gov. The plots in this thesis were produced with Matplotlib (Hunter, 2007).

References

Akasofu, S. I. (1964), 'The development of the auroral substorm', *Planetary and Space Science* **12**(4), 273–282.
URL: *http://dx.doi.org/10.1016/0032-0633(64)90151-5*

Baker, D. N., Kanekal, S. G., Hoxie, V. C., Batiste, S., Bolton, M., Li, X., Elkington, S. R., Monk, S., Reukauf, R., Steg, S., Westfall, J., Belting, C., Bolton, B., Braun, D., Cervelli, B., Hubbell, K., Kien, M., Knappmiller, S., Wade, S., Lamprecht, B., Stevens, K., Wallace, J., Yehle, A., Spence, H. E. and Friedel, R. (2013), 'The Relativistic Electron-Proton Telescope (REPT) instrument on board the Radiation Belt Storm Probes (RBSP) spacecraft: Characterization of earth's radiation belt high-energy particle populations'.
URL: *http://dx.doi.org/10.1007/s11214-012-9950-9*

Bingham, S. T., Mouikis, C. G., Kistler, L. M., Boyd, A. J., Paulson, K., Farrugia, C. J., Huang, C. L., Spence, H. E., Claudepierre, S. G. and Kletzing, C. (2018), 'The Outer Radiation Belt Response to the Storm Time Development of Seed Electrons and Chorus Wave Activity During CME and CIR Driven Storms', *Journal of Geophysical Research: Space Physics* **123**(12), 10,139–10,157.
URL: *http://dx.doi.org/10.1029/2018JA025963*

Cyamukungu, M., Benck, S., Borisov, S., Gregoire, G., Cabrera, J., Bonnet, J. L., Desoete, B., Preudrhomme, F., Semaille, C., Creve, G., Saedeleer, J. D., Ilsen, S., De Busser, L., Pierrard, V., Bonnewijn, S., Maes, J., Ransbeeck, E. V., Neefs, E., Lemaire, J., Valtonen, E., Punkkinen, R., Anciaux, M., Litefti, K., Brun, N., Pauwels, D., Quevrin, C., Moreau, D., Helderweirt, A., Hajdas, W. and Nieminen, P. (2014), 'The energetic particle telescope (EPT) on board PROBA-V: Description of a new science-class instrument for particle detection in space', *IEEE Transactions on Nuclear Science* **61**(6), 3667–3681.
URL: *http://dx.doi.org/10.1109/TNS.2014.2361955*

Daglis, I. A., Thorne, R. M., Baumjohann, W. and Orsini, S. (1999), 'The terrestrial ring current: Origin, formation, and decay'.
URL: *http://dx.doi.org/10.1029/1999RG900009*

ESA/Image Gallery (2016), `https://www.esa.int/ESA_Multimedia/Images/2016/06/Illustration_showing_Van_Allen_radiation_belts`. Accessed: 2021-03-11.

ESA Proba Missions (n.d.), `http://www.esa.int/Enabling_Support/Space_Engineering_Technology/Proba_Missions`. Accessed: 2021-02-24.

Geomagnetic AE index (2015). World Data Center for Geomagnetism, Kyoto, M. Nose, T. Iyemori, M. Sugiura, T. Kamei (2015), Geomagnetic AE index.
URL: *http://dx.doi.org/10.17593/15031-54800*

Geomagnetic Dst index (2015). World Data Center for Geomagnetism, Kyoto, M. Nose, T. Iyemori, M. Sugiura, T. Kamei (2015), Geomagnetic Dst index.
URL: *http://dx.doi.org/10.17593/14515-74000*

Gieseler, J., Oleynik, P., Hietala, H., Vainio, R., Hedman, H. P., Peltonen, J., Punkkinen, A., Punkkinen, R., Säntti, T., Hæggström, E., Praks, J., Niemelä, P., Riwanto, B., Jovanovic, N. and Mughal, M. R. (2020), 'Radiation monitor RADMON aboard Aalto-1 CubeSat: First results', *Advances in Space Research* **66**(1), 52–65.
URL: *https://doi.org/10.1016/j.asr.2019.11.023*

Gieseler, J., Oleynik, P., Hietala, H., Vainio, R., Hedman, H.-P., Peltonen, J., Punkkinen, A., Punkkinen, R., Säntti, T., Hæggström, E., Praks, J., Niemelä, P., Riwanto, B., Jovanovic, N. and Mughal, M. R. (2019), 'Aalto-1/radmon data set 2017/2018'.
URL: *https://doi.org/10.5281/zenodo.3541628*

Goldstein, H. (1980), *Classical Mechanics*, Addison-Wesley.

Gonzalez, W. D., Joselyn, J. A., Kamide, Y., Kroehl, H. W., Rostoker, G., Tsurutani, B. T. and Vasyliunas, V. M. (1994), 'What is a geomagnetic storm?', *Journal of Geophysical Research* **99**(A4), 5771.
URL: *http://dx.doi.org/10.1029/93ja02867*

Horne, R. B., Lam, M. M. and Green, J. C. (2009), 'Energetic electron precipitation from the outer radiation belt during geomagnetic storms', *Geophysical Research Letters* **36**(19), L19104.
URL: *http://doi.wiley.com/10.1029/2009GL040236*

Hunter, J. D. (2007), 'Matplotlib: A 2d graphics environment', *Computing in Science & Engineering* **9**(3), 90–95.
URL: *http://dx.doi.org/10.1109/MCSE.2007.55*

Kamide, Y., Baumjohann, W., Daglis, I. A., Gonzalez, W. D., Grande, M., Joselyn, J. A., McPherron, R. L., Phillips, J. L., Reeves, E. G. D., Rostoker, G., Sharma, A. S., Singer, H. J., Tsurutani, B. T. and Vasyliunas, V. M. (1998), 'Current understanding of magnetic storms: Storm-substorm relationships', *Journal of Geophysical Research: Space Physics* **103**(A8), 17705–17728.
URL: *http://doi.wiley.com/10.1029/98JA01426*

Kestilä, A., Tikka, T., Peitso, P., Rantanen, J., Näsilä, A., Nordling, K., Saari, H., Vainio, R., Janhunen, P., Praks, J. and Hallikainen, M. (2013), 'Aalto-1 nanosatellite – technical description and mission objectives', *Geoscientific Instrumentation, Methods and Data Systems* **2**(1), 121–130.
URL: *http://dx.doi.org/10.5194/gi-2-121-2013*

Kilpua, E. and Koskinen, H. (2017), *Introduction to Plasma Physics*, 1 edn, LIMES, Finland.

King, J. H. and Papitashvili, N. E. (2005), 'Solar wind spatial scales in and comparisons of hourly Wind and ACE plasma and magnetic field data', *Journal of Geophysical Research: Space Physics* **110**(A2), A02104.
URL: *http://doi.wiley.com/10.1029/2004JA010649*

Koskinen, H. (2011), *Physics of Space Storms: From the Solar Surface to the Earth*, Springer-Verlag, Germany.

Laundal, K. M. and Richmond, A. D. (2017), 'Magnetic Coordinate Systems', *Space Science Reviews* **206**(1-4), 27–59.
URL: *http://dx.doi.org/10.1007/s11214-016-0275-y*

Li, W. and Hudson, M. K. (2019), 'Earth's Van Allen Radiation Belts: From Discovery to the Van Allen Probes Era', *Journal of Geophysical Research: Space Physics* **124**(11), 8319–8351.
URL: *http://dx.doi.org/10.1029/2018JA025940*

Lyons, L. R. and Thorne, R. M. (1973), 'Equilibrium structure of radiation belt electrons', *Journal of Geophysical Research* **78**(13), 2142–2149.
URL: *http://doi.wiley.com/10.1029/JA078i013p02142*

Mauk, B. H., Fox, N. J., Kanekal, S. G., Kessel, R. L., Sibeck, D. G. and Ukhorskiy, A. (2013), 'Science objectives and rationale for the radiation belt storm probes mission'.
URL: *http://dx.doi.org/10.1007/s11214-012-9908-y*

McIlwain, C. E. (1961), 'Coordinates for mapping the distribution of magnetically trapped particles', *Journal of Geophysical Research* **66**(11), 3681–3691.
URL: *http://doi.wiley.com/10.1029/JZ066i011p03681*

Merka, J., Szabo, A., Slavin, J. A. and Peredo, M. (2005), 'Three-dimensional position and shape of the bow shock and their variation with upstream Mach numbers and interplanetary magnetic field orientation', *Journal of Geophysical Research: Space Physics* **110**(A4).
URL: *http://doi.wiley.com/10.1029/2004JA010944*

Millan, R. M. and Thorne, R. M. (2007), 'Review of radiation belt relativistic electron losses', *Journal of Atmospheric and Solar-Terrestrial Physics* **69**, 362–377.
URL: *http://dx.doi.org/10.1016/j.jastp.2006.06.019*

Mughal, M. R., Praks, J., Vainio, R., Janhunen, P., Envall, J., Näsilä, A., Oleynik, P., Niemelä, P., Slavinskis, A., Gieseler, J., Jovanovic, N., Riwanto, B., Toivanen, P., Leppinen, H., Tikka, T., Punkkinen, A., Punkkinen, R., Hedman, H.-P., Lill, J.-O. and Slotte, J. (2021), 'Aalto-1, multi-payload CubeSat: In-orbit results and lessons learned', *Acta Astronautica* .
URL: *http://dx.doi.org/10.1016/j.actaastro.2020.11.044*

NASA/Goddard/Aaron Kaase (2017), `https://www.nasa.gov/mission_pages/sunearth/multimedia/magnetosphere.html`. Accessed: 2021-03-03.

Oleynik, P., Vainio, R., Punkkinen, A., Dudnik, O., Gieseler, J., Hedman, H. P., Hietala, H., Hæggström, E., Niemelä, P., Peltonen, J., Praks, J., Punkkinen, R., Säntti, T. and Valtonen, E. (2020), 'Calibration of RADMON radiation monitor onboard Aalto-1 CubeSat', *Advances in Space Research* **66**(1), 42–51.
URL: *https://doi.org/10.1016/j.asr.2019.11.020*

Parker, E. N. (1958), 'Dynamics of the Interplanetary Gas and Magnetic Fields.', *The Astrophysical Journal* **128**, 664.
URL: *https://doi.org/10.1086/146579*

Partamies, N., Juusola, L., Tanskanen, E. and Kauristie, K. (2013), 'Statistical properties of substorms during different storm and solar cycle phases', *Annales Geophysicae* **31**(2), 349–358.
URL: *http://dx.doi.org/10.5194/angeo-31-349-2013*

Peltonen, J., Hedman, H., Ilmanen, A., Lindroos, M., Määttänen, M., Pesonen, J., Punkkinen, R., Punkkinen, A., Vainio, R., Valtonen, E., Săntti, T., Pentikäinen, J. and Hæggström, E. (2014), Electronics for the radmon instrument on the aalto-1 student satellite, *in* '10th European Workshop on Microelectronics Education (EWME)', pp. 161–166.
URL: *http://dx.doi.org/10.1109/EWME.2014.6877418*

Peredo, M., Slavin, J. A., Mazur, E. and Curtis, S. A. (1995), 'Three-dimensional position and shape of the bow shock and their variation with Alfvénic, sonic and magnetosonic Mach numbers and interplanetary magnetic field orientation', *Journal of Geophysical Research* **100**(A5), 7907.
URL: *http://doi.wiley.com/10.1029/94JA02545*

Pierrard, V., Botek, E., Ripoll, J. F. and Cunningham, G. (2020), 'Electron Dropout Events and Flux Enhancements Associated With Geomagnetic Storms Observed

by PROBA-V/Energetic Particle Telescope From 2013 to 2019', *Journal of Geophysical Research: Space Physics* **125**(12), e2020JA028487.
URL: *http://dx.doi.org/10.1029/2020JA028487*

Pierrard, V., Lopez Rosson, G., Borremans, K., Lemaire, J., Maes, J., Bonnewijn, S., Van Ransbeeck, E., Neefs, E., Cyamukungu, M., Benck, S., Bonnet, L., Borisov, S., Cabrera, J., Grégoire, G., Semaille, C., Creve, G., De Saedeleer, J., Desoete, B., Preud'homme, F., Anciaux, M., Helderweirt, A., Litefti, K., Brun, N., Pauwels, D., Quevrin, C., Moreau, D., Punkkinen, R., Valtonen, E., Hajdas, W. and Nieminen, P. (2014), 'The Energetic Particle Telescope: First Results', *Space Science Reviews* **184**(1-4), 87–106.
URL: *http://dx.doi.org/10.1007/s11214-014-0097-8*

Pirjola, R. (2000), 'Geomagnetically induced currents during magnetic storms', *IEEE Transactions on Plasma Science* **28**(6), 1867–1873.
URL: *http://dx.doi.org/10.1109/27.902215*

Praks, J., Mughal, M. R., Vainio, R., Janhunen, P., Envall, J., Oleynik, P., Näsilä, A., Leppinen, H., Niemelä, P., Slavinskis, A., Gieseler, J., Toivanen, P., Tikka, T., Peltola, T., Bosser, A., Schwarzkopf, G., Jovanovic, N., Riwanto, B., Kestilä, A., Punkkinen, A., Punkkinen, R., Hedman, H.-P., Säntti, T., Lill, J.-O., Slotte, J., Kettunen, H. and Virtanen, A. (2021), 'Aalto-1, multi-payload CubeSat: Design, integration and launch', *Acta Astronautica* .
URL: *https://doi.org/10.1016/j.actaastro.2020.11.042*

RBSP-ECT Science and Data Portal (n.d.). Radiation Belt Storm Probes Energetic Particle Composition & Thermal Plasma Suite, Science Operations and Data Center.
URL: *https://rbsp-ect.newmexicoconsortium.org/rbsp_ect.php*

Reeves, G. D., McAdams, K. L., Friedel, R. H. W. and O'Brien, T. P. (2003), 'Acceleration and loss of relativistic electrons during geomagnetic storms', *Geophysical Research Letters* **30**(10).
URL: *http://dx.doi.org/10.1029/2002gl016513*

Reeves, G. D., Spence, H. E., Henderson, M. G., Morley, S. K., Friedel, R. H., Funsten, H. O., Baker, D. N., Kanekal, S. G., Blake, J. B., Fennell, J. F., Claudepierre, S. G., Thorne, R. M., Turner, D. L., Kletzing, C. A., Kurth, W. S., Larsen, B. A. and Niehof, J. T. (2013), 'Electron acceleration in the heart of the Van Allen radiation belts', *Science* **341**(6149), 991–994.
URL: *https://doi.org/10.1126/science.1237743*

Richardson, I. G. (2018), 'Solar wind stream interaction regions throughout the heliosphere'.
URL: *https://doi.org/10.1007/s41116-017-0011-z*

Shue, J. H. (1997), 'A new functional form to study the solar wind control of the magnetopause size and shape', *Journal of Geophysical Research A: Space Physics* **102**(A5), 9497–9511.
URL: *http://dx.doi.org/10.1029/97JA00196*

Shue, J.-H., Song, P., Russell, C. T., Steinberg, J. T., Chao, J. K., Zastenker, G., Vaisberg, O. L., Kokubun, S., Singer, H. J., Detman, T. R. and Kawano, H. (1998), 'Magnetopause location under extreme solar wind conditions', *Journal of Geophysical Research: Space Physics* **103**(A8), 17691–17700.
URL: *http://dx.doi.org/10.1029/98ja01103*

Spence, H. E., Reeves, G. D., Baker, D. N., Blake, J. B., Bolton, M., Bourdarie, S., Chan, A. A., Claudepierre, S. G., Clemmons, J. H., Cravens, J. P., Elkington, S. R., Fennell, J. F., Friedel, R. H., Funsten, H. O., Goldstein, J., Green, J. C., Guthrie, A., Henderson, M. G., Horne, R. B., Hudson, M. K., Jahn, J. M., Jordanova, V. K., Kanekal, S. G., Klatt, B. W., Larsen, B. A., Li, X., MacDonald, E. A., Mann, I. R., Niehof, J., O'Brien, T. P., Onsager, T. G., Salvaggio, D., Skoug, R. M., Smith, S. S., Suther, L. L., Thomsen, M. F. and Thorne, R. M. (2013), 'Science goals and overview of the Radiation Belt Storm Probes (RBSP) energetic particle, composition, and thermal plasma (ECT) suite on NASA's van allen probes mission'.
URL: *http://dx.doi.org/10.1007/s11214-013-0007-5*

Sullivan, J. D. (1971), 'Geometric factor and directional response of single and multi-element particle telescopes', *Nuclear Instruments and Methods* **95**(1), 5–11.
URL: *http://dx.doi.org/10.1016/0029-554X(71)90033-4*

Turner, D. L., Kilpua, E. K. J., Hietala, H., Claudepierre, S. G., O'Brien, T. P., Fennell, J. F., Blake, J. B., Jaynes, A. N., Kanekal, S., Baker, D. N., Spence, H. E., Ripoll, J. and Reeves, G. D. (2019), 'The Response of Earth's Electron Radiation Belts to Geomagnetic Storms: Statistics From the Van Allen Probes Era Including Effects From Different Storm Drivers', *Journal of Geophysical Research: Space Physics* **124**(2), 1013–1034.
URL: *http://dx.doi.org/10.1029/2018JA026066*

Turner, D. L., O'Brien, T. P., Fennell, J. F., Claudepierre, S. G., Blake, J. B., Kilpua, E. K. J. and Hietala, H. (2015), 'The effects of geomagnetic storms on electrons in Earth's radiation belts', *Geophysical Research Letters* **42**(21), 9176–9184.
URL: *http://doi.wiley.com/10.1002/2015GL064747*

Van Allen, J. A., Ludwig, G. H., Ray, E. C. and McIlwain, C. E. (1958), 'Observation of High Intensity Radiation by Satellites 1958 Alpha and Gamma', *Journal of Jet*

Propulsion **28**(9), 588–592.
URL: *http://dx.doi.org/10.2514/8.7396*

Wanliss, J. A. (2007), When is it alright to use SYM-H as a storm index?, *in* 'AGU Fall Meeting Abstracts', Vol. 2007, pp. SM32A–05.
URL: *https://ui.adsabs.harvard.edu/abs/2007AGUFMSM32A..05W*